RESEARCH ARTICLE

MYC Induces Oncogenic Stress through RNA Decay and Ribonucleotide Catabolism in Breast Cancer

Jitendra K. Meena[1,2], Jarey H. Wang[2,4], Nicholas J. Neill[1,2,3], Dianne Keough[8], Nagireddy Putluri[5], Panagiotis Katsonis[3], Amanda M. Koire[3], Hyemin Lee[6], Elizabeth A. Bowling[1,2], Siddhartha Tyagi[2], Mayra Orellana[2], Rocio Dominguez-Vidaña[2], Heyuan Li[2], Kenneth Eagle[3], Charles Danan[3], Hsiang-Ching Chung[2], Andrew D. Yang[1,2,3,4], William Wu[2,4], Sarah J. Kurley[2], Brian M. Ho[2,4], Joseph R. Zoeller[1,2,4], Calla M. Olson[1,2], Kristen L. Meerbrey[1,2], Olivier Lichtarge[3], Arun Sreekumar[5], Clifford C. Dacso[5], Luke W. Guddat[8], Dominik Rejman[7], Dana Hocková[7], Zlatko Janeba[7], Lukas M. Simon[1], Charles Y. Lin[1,2,3,9], Monica C. Pillon[1,2], and Thomas F. Westbrook[1,2,3,9]

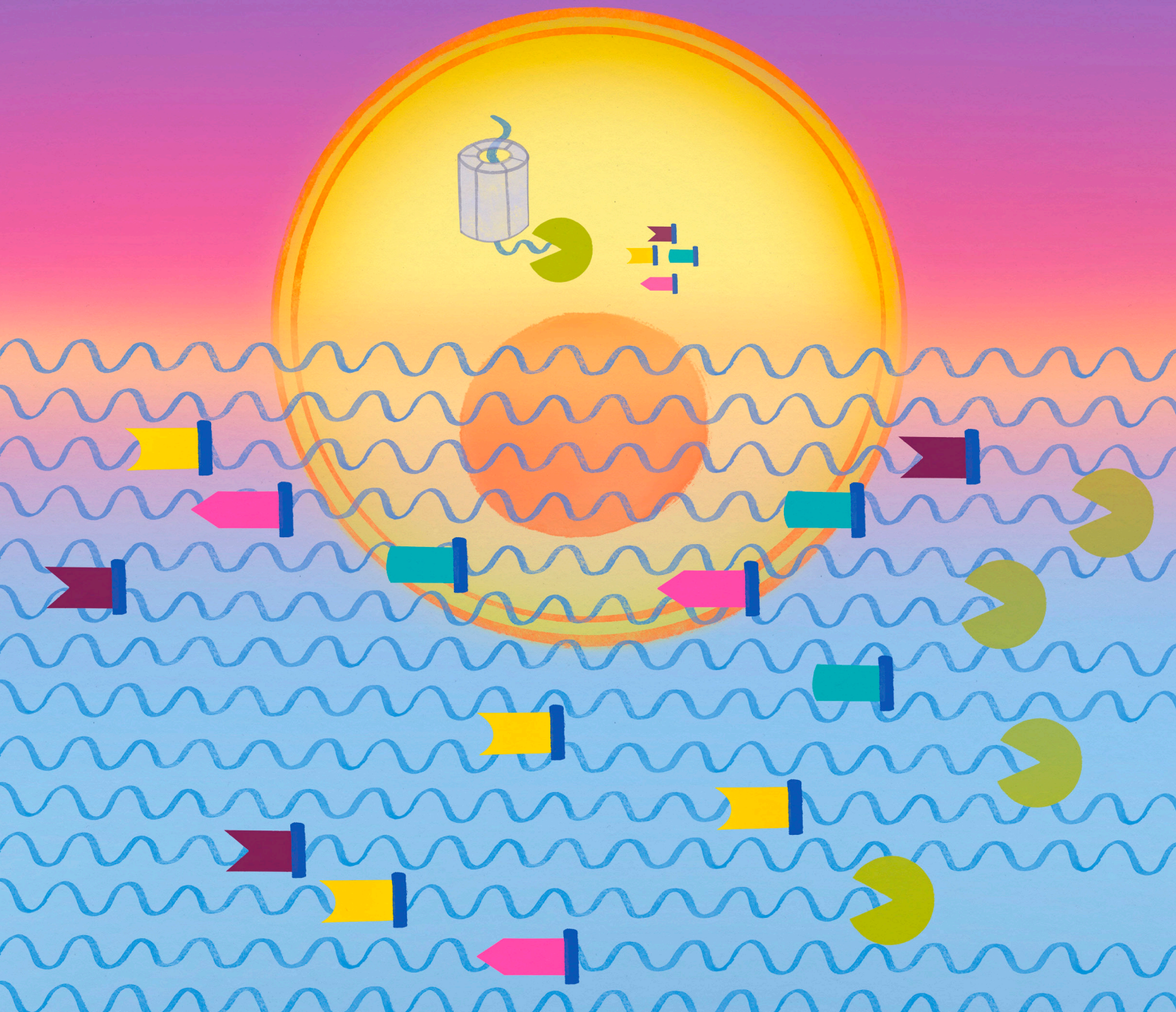

ABSTRACT Upregulation of MYC is a hallmark of cancer, wherein MYC drives oncogenic gene expression and elevates total RNA synthesis across cancer cell transcriptomes. Although this transcriptional anabolism fuels cancer growth and survival, the consequences and metabolic stresses induced by excess cellular RNA are poorly understood. Herein, we discover that RNA degradation and downstream ribonucleotide catabolism is a novel mechanism of MYC-induced cancer cell death. Combining genetics and metabolomics, we find that MYC increases RNA decay through the cytoplasmic exosome, resulting in the accumulation of cytotoxic RNA catabolites and reactive oxygen species. Notably, tumor-derived exosome mutations abrogate MYC-induced cell death, suggesting excess RNA decay may be toxic to human cancers. In agreement, purine salvage acts as a compensatory pathway that mitigates MYC-induced ribonucleotide catabolism, and inhibitors of purine salvage impair MYC$^+$ tumor progression. Together, these data suggest that MYC-induced RNA decay is an oncogenic stress that can be exploited therapeutically.

SIGNIFICANCE: MYC is the most common oncogenic driver of poor-prognosis cancers but has been recalcitrant to therapeutic inhibition. We discovered a new vulnerability in MYC+ cancer where MYC induces cell death through excess RNA decay. Therapeutics that exacerbate downstream ribonucleotide catabolism provide a therapeutically tractable approach to TNBC (Triple-negative Breast Cancer) and other MYC-driven cancers.

INTRODUCTION

During tumorigenesis, cancer cells acquire genetic and epigenetic alterations that lead to widespread reprogramming of transcriptional and metabolic processes. Such changes fuel uncontrolled proliferation and other protumor hallmarks (1–6). However, large-scale deregulation of these processes may also create new dependencies and vulnerabilities in cancer cells (5, 7). In some cases, these counterbalancing protumor and stress hallmarks result from the same oncogenic alteration. MYC is a salient example of an oncogene that induces stresses across multiple cellular processes, from DNA replication to energy metabolism, that may be exploited for anticancer therapies (8–12).

Amplification and/or hyperactivation of *MYC* occurs in 20% to 40% of human malignancies and is associated with poor prognoses. As a transcription factor, MYC regulates many of its protumor functions by inducing or repressing gene expression programs (13–19). Oncogenic MYC activation has also been shown to elevate total RNA and protein production in many disease contexts to support the metabolic demands of cell growth and proliferation; the mechanisms for this elevation in macromolecular synthesis are subjects of intensive study (20–30).

While MYC-driven increased production of cellular RNA endows cancer cells with proliferative advantages, such a widespread increase in RNA synthesis may also create a burden on cells to maintain homeostasis of these macromolecules (23, 24, 30). For instance, MYC-driven cancers support the metabolic demands of increased transcription by increasing expression of *de novo* nucleotide biosynthesis pathways (31–34). In contrast, much less is known about how such elevated RNA synthesis is counterbalanced by RNA decay pathways and how this impacts downstream catabolic pathways that handle RNA breakdown products.

Here, we demonstrate that increased production of RNA catabolites and catabolic byproducts such as reactive oxygen species (ROS) is a critical source of MYC-induced cell death and oncogenic stress. In the setting of MYC hyperactivation, the RNA exosome and its catalytic ribonuclease DIS3L contributes to oncogenic cell death by facilitating increased RNA decay and subsequent accumulation of RNA catabolites. DIS3L mutations observed in human cancers can compromise this function of *DIS3L* and disable MYC-driven cell death. Furthermore, we find that purine salvage, which counterbalances

[1]Therapeutic Innovation Center (THINC), Baylor College of Medicine, Houston, Texas. [2]Verna & Marrs McLean Department of Biochemistry and Molecular Pharmacology, Baylor College of Medicine, Houston, Texas. [3]Department of Molecular and Human Genetics, Baylor College of Medicine, Houston, Texas. [4]Medical Scientist Training Program, Baylor College of Medicine, Houston, Texas. [5]Department of Molecular and Cellular Biology, Baylor College of Medicine, Houston, Texas. [6]Department of Experimental Radiation Oncology, The University of Texas MD Anderson Cancer Center, Houston, Texas. [7]Institute of Organic Chemistry and Biochemistry of the Czech Academy of Sciences, Prague, Czech Republic. [8]The School of Chemistry and Molecular Biosciences, The University of Queensland, Brisbane, Australia. [9]Dan L Duncan Comprehensive Cancer Center, Baylor College of Medicine, Houston, Texas.

Current address for C.Y. Lin: Kronos Bio, Cambridge, MA; current address for C. Danan: Perelman School of Medicine, University of Pennsylvania, Philadelphia, Pennsylvania; current address for K. Eagle: Ken Eagle Consulting, Houston, Texas; and current address for A.M. Koire: Harvard Medical School, Boston, Massachusetts and Department of Psychiatry, Brigham and Women's Hospital, Boston, Massachusetts.

Corresponding Authors: Thomas F. Westbrook, Department of Biochemistry & Molecular Pharmacology, Baylor College of Medicine, One Baylor Plaza, Houston, TX 77030. E-mail: thomasw@bcm.edu; and Jitendra K. Meena, meena@bcm.edu

Cancer Discov 2024;14:1699–716

doi: 10.1158/2159-8290.CD-22-0649

ribonucleotide catabolism, is a compensatory mechanism on which MYC-driven cancers become dependent to tolerate such catabolic stress. MYC-driven breast cancers are especially sensitive to genetic and pharmacologic inhibition of purine salvage, which may represent a new therapeutic approach.

RESULTS

Oncogenic MYC Stimulates RNA Decay and Accumulation of RNA Catabolites

In many cell lineages and experimental systems, oncogenic activation of MYC has been shown to amplify the synthesis of cellular RNA through direct and indirect mechanisms (25, 26, 35–39). Several important studies have demonstrated that MYC-driven cancers support the metabolic demand of this global increase in RNA synthesis through coordinated transcriptional and translational control of nucleotide synthesis (23, 24, 30). These MYC programs have been the subject of intense therapeutic discovery (23, 40). In contrast, the impact of *MYC*-amplified RNA synthesis on downstream RNA decay and ribonucleotide catabolism in cancer and how this impacts tumor cell fitness is largely unknown.

To determine if MYC-driven tumors have altered ribonucleotide catabolism, we analyzed 61 primary human breast cancers for which broad metabolomics profiling was previously performed (32). Primary tumors were separated into MYC-high and MYC-low subsets via a MYC transcriptional signature (41) and assessed for levels of nucleic acid metabolites (Fig. 1A; Supplementary Fig. S1A–S1C). Nucleic acid metabolites, including those specific to nucleotide catabolism, such as uracil and β-alanine, were significantly more abundant in MYC-high breast cancers (Fig. 1A; Supplementary Fig. S1A–S1C). Strikingly, MYC-high breast cancers exhibited significantly higher levels of catabolites selective to RNA breakdown (i.e., not DNA breakdown), such as xanthosine, suggesting that RNA degradation is elevated in MYC-driven tumors.

To assess more directly whether MYC hyperactivation alters the accumulation of ribonucleotide catabolites, we performed targeted metabolomics profiling of human mammary epithelial cells (HMEC) expressing the MYC-estrogen receptor fusion protein, in which MYC activity can be rapidly induced with 4-hydroxytamoxifen (4-OHT; Supplementary Fig. S1D). Aberrant activation of MYC increased the abundance of nucleosides and free bases that may result from RNA or DNA degradation (e.g., xanthine, uracil, and β-alanine; Fig. 1B–E). Importantly, MYC also increased ribonucleotide catabolites specific to RNA degradation (e.g., xanthosine) and the end products of nucleotide degradation (e.g., uric acid). Prior reports suggest eukaryotic RNA turnover is at least 10- to 100-fold higher than that of DNA (43–46), leading us to hypothesize that after MYC hyperactivation, the increase in nucleotide catabolites was primarily the consequence of increased RNA degradation (as opposed to DNA degradation). This prediction was also supported by mathematical modeling of purine metabolism (46, 47), where increasing total cellular RNA by 25% led to a robust increase in hypoxanthine (~4 to 11 fold) and xanthine (~4 to 6 fold) concentration within 5 to 8 hours but increasing DNA by 25% did not impact hypoxanthine and xanthine concentrations (Supplementary Fig. S1E–S1G). To directly test whether oncogenic MYC affected global RNA decay, we labeled nascent RNA with the uridine analog 5-ethynyl uridine (EU) and quantified RNA synthesis (through EU incorporation) and RNA decay (through pulse-chase experiments; Fig. 1F). In agreement with the reported role of MYC in enhancing cellular RNA synthesis, MYC induction resulted in increased nascent RNA production as measured by fluorescent detection of EU immediately following EU labeling (Fig. 1G). Importantly, pulse-chase quantification of EU-labeled RNA over time revealed an increase in RNA decay rate in the MYC-hyperactivated state (Fig. 1H), suggesting that MYC hyperactivation increases both global RNA synthesis and RNA decay.

Taken together, these results indicate that MYC hyperactivation leads to an increase in RNA decay and a concomitant accumulation of many ribonucleotide catabolic intermediaries and terminal products. Furthermore, ribonucleotide catabolites are elevated in MYC-driven breast cancers, suggesting that this imbalance in RNA decay exists in the context of oncogenic MYC hyperactivation.

The Cytoplasmic RNA Exosome Mediates MYC-Induced Cell Death

MYC-driven oncogenic stress pathways and cell death have been shown to be major barriers to tumorigenesis. Notably, in addition to accumulation of RNA catabolites, MYC induction also led to a significant increase in cell death, including apoptosis (Supplementary Fig. S1H–S1J). As some RNA catabolic products can be cytotoxic (48–50), these findings led us to investigate whether heightened RNA decay and ribonucleotide catabolism contribute to MYC-driven cell death and thus may be a form of oncogenic stress. More specifically, we hypothesized that regulators of RNA degradation may impact cell survival in the setting of MYC hyperactivation.

To investigate whether pathways that control RNA decay can also impact cell survival in the context of oncogenic MYC hyperactivation, we analyzed genome-wide loss-of-function screen data we previously conducted in HMECs with and without MYC hyperactivation (10, 51). In particular, we were interested in genes whose knockdown increased cell viability selectively upon MYC induction. These genes may encode proteins that are critical facilitators of MYC-induced oncogenic stress. Thus, short hairpin RNAs (shRNA) targeting these genes would result in decreased MYC-induced cell death, resulting in greater shRNA abundance specifically in the MYC-induced cell population (Fig. 2A). A total of 223 genes (Supplementary Fig. S1K; Supplementary Table S1) were identified as candidate facilitators of MYC-induced cell death (genes identified had 2+ shRNAs per gene with a log2 fold change >0.5 in MYC-induced state compared to MYC-normal state, and $P < 0.1$). To systematically identify cellular components that participate in MYC-induced cell death, we performed gene ontology analysis (52). Notably, from these 223 candidates, the top scoring protein complex was the cytoplasmic RNA exosome, a multi-subunit complex that executes exonucleolytic decay of single-strand RNA in the 3′-5′ direction into single nucleotides (Fig. 2B and C; Supplementary Fig. S1E; Supplementary Table S2). This highlighted the hypothesis that the RNA exosome may be a conduit of cellular stress in context of MYC hyperactivation by increasing cellular accumulation of RNA breakdown products. Multiple shRNAs targeting

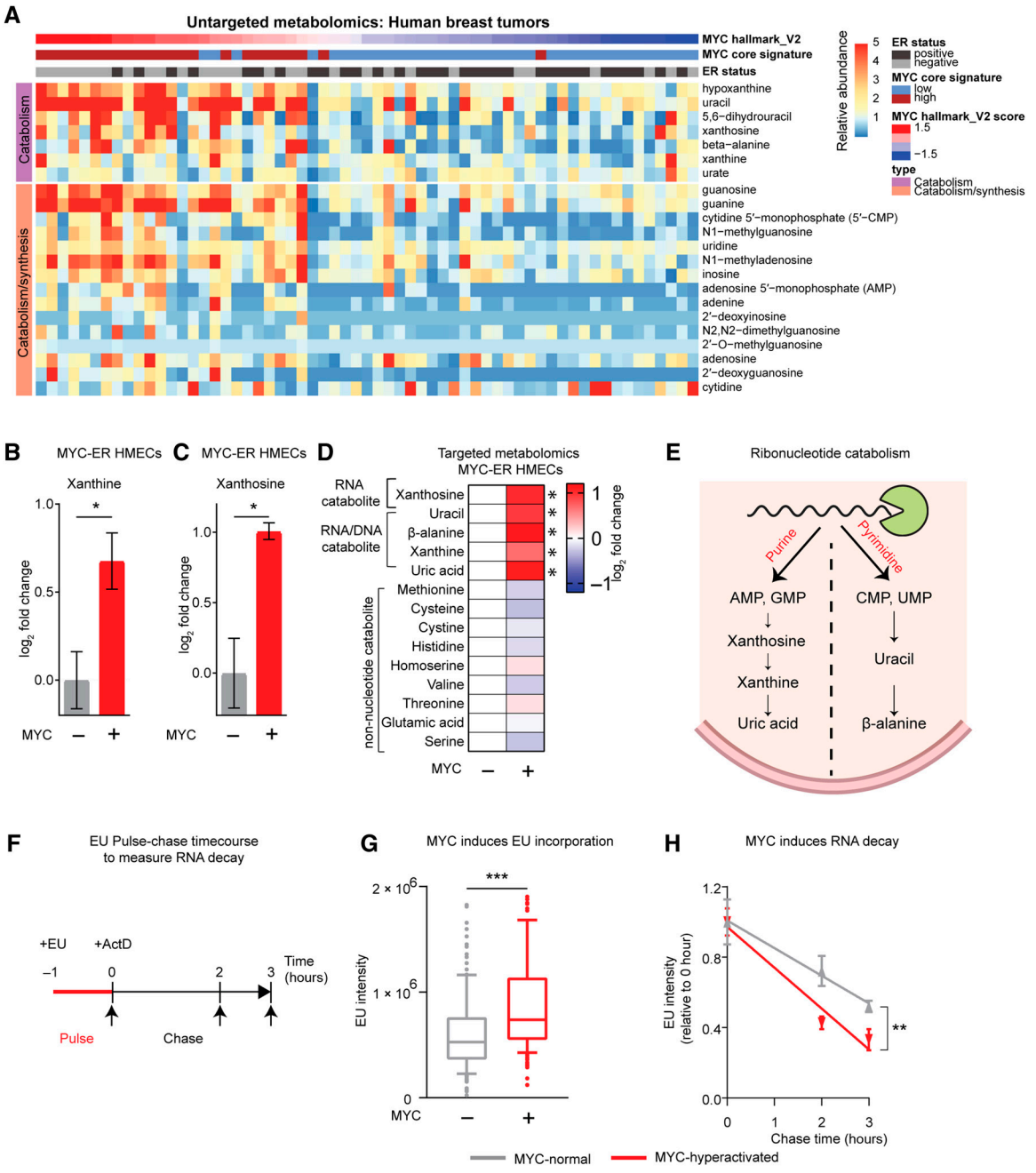

Figure 1. Oncogenic MYC stimulates widespread RNA decay and accumulation of RNA catabolites. **A,** MYC-hyperactivated breast tumors exhibit elevated accumulation of RNA degradation–related nucleotide catabolites. Primary human breast cancers ($n = 61$) and matched normal adjacent tissue were previously profiled via untargeted metabolomics and microarray (32). Herein, tumors were stratified by MYC hyperactivation gene signatures (denoted with two independently derived MYC hyperactivation gene signatures shown on top bars). Shown is a heatmap of nucleotide metabolites. Metabolites that are exclusively derived from RNA/DNA breakdown ("catabolism") are shown in top rows; metabolites that can result from synthetic or catabolic pathways are shown in bottom rows. Heatmap data displayed as fold-change of metabolite abundance compared to the average of matched adjacent normal tissue. MYC-signature scores were derived from tumor gene expression data using MYC core signature and MYC hallmark_V2 (41, 42). **B–D,** Oncogenic MYC induces accumulation of RNA catabolites. HMECs engineered with MYC-ER were induced for MYC hyperactivation (±60 nmol/L 4-OHT for 4 hours) and analyzed by targeted metabolomics. Two representative catabolites that arise from degradation of RNA or DNA [Xanthine, (**B**)] or from degradation selectively from RNA [Xanthosine, (**C**)] are shown (data are mean ± SEM, $n = 3$). **D,** Heatmap of metabolites in MYC-ER HMECs show log2 fold change in RNA catabolites in MYC-hyperactivated conditions relative to MYC-normal (data are mean of three biological replicates). **E,** Model of ribonucleotide catabolism resulting from RNA decay. **F,** Schematic for measuring RNA decay. Cells were incubated ±60 nmol/L 4-OHT to induce MYC-ER, incubated with EU for 1 hour, and then washed out to remove EU. Samples were collected at time 0 to measure EU incorporation (RNA synthesis) and at 2 or 3 hours post-chase to measure RNA decay. **G,** Boxplot of EU intensity in MYC-ER HMECs shows increased EU incorporation in MYC-hyperactivated state after 1 hour of EU labeling ($n > 100$ cells per group). **H,** MYC induces RNA decay. Measurements of EU intensity in MYC-ER HMECs at indicated timepoints after removal of EU (chase). Linear regression indicates faster decay of EU-labeled RNA in MYC-hyperactivated conditions ($n > 100$ cells per group). Significance was analyzed by two-tailed, unpaired Student t test for **B**, **C**, and **G**; slopes for **H** were compared using GraphPad Prism's simple linear regression. *, $P < 0.05$; **, $P < 0.01$; ***, $P < 0.001$.

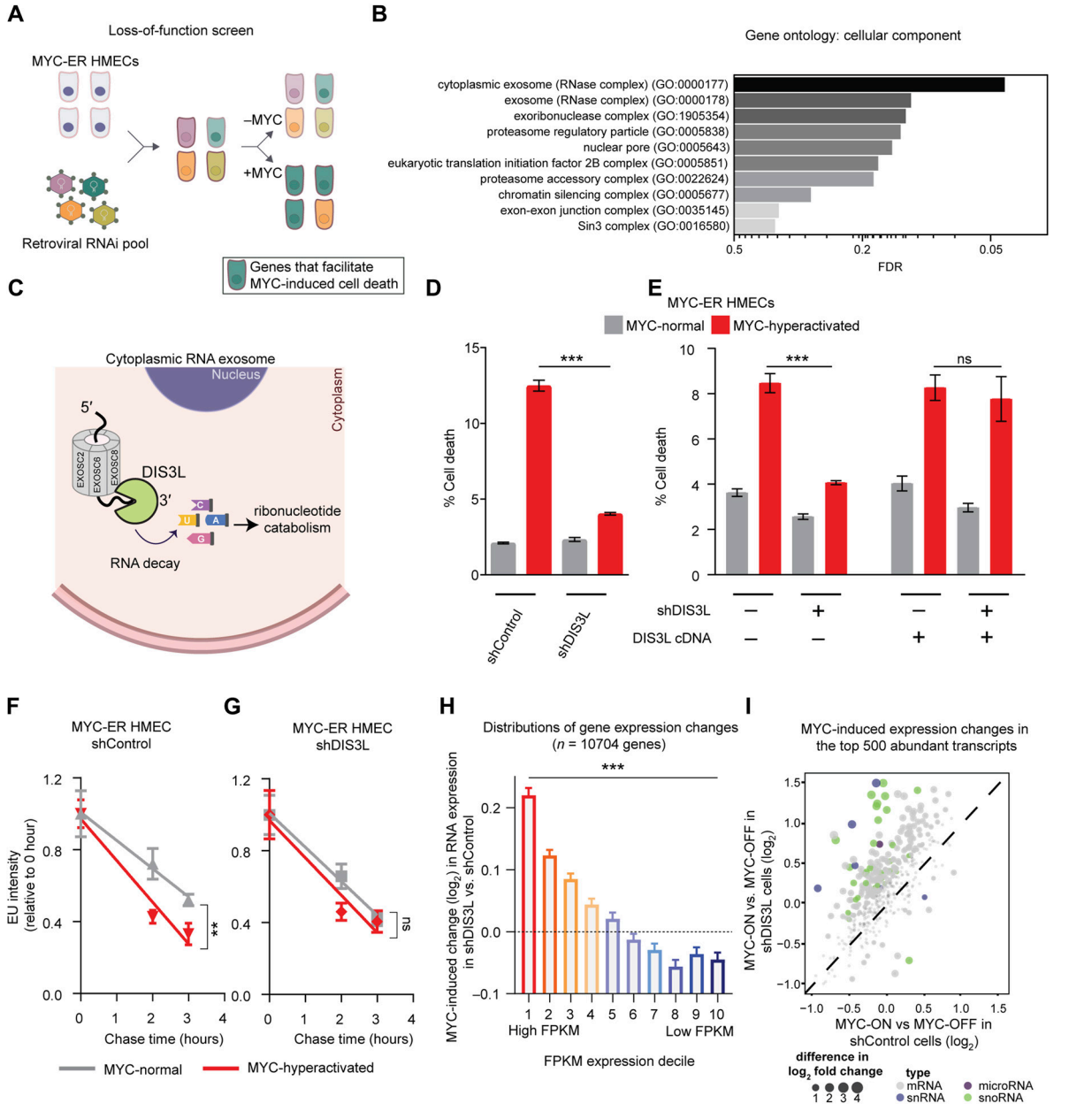

Figure 2. The cytoplasmic RNA exosome mediates MYC-induced RNA decay and cell death. **A,** Schematic of loss-of-function shRNA screen in MYC-ER HMECs to identify genes required for MYC-induced cell death. **B,** Gene ontology of enriched cellular components and complexes among the candidate genes (223 genes) required for MYC-induced cell death identified from the shRNA screen. Gene ontology performed using PANTHER (86). FDR shown for pathways with >2-fold enrichment. **C,** Model illustrating cytoplasmic exosome-driven RNA decay. DIS3L is the catalytic component of cytoplasmic exosome, which degrades single-strand RNA in 3′-5′ direction, producing ribonucleotides that are further processed in catabolic pathways. **D,** MYC-induced cell death requires DIS3L. MYC-ER HMECs were engineered with and without DIS3L depletion. Cell viability was analyzed by PI staining 24 hours after MYC hyperactivation with 60 nmol/L 4-OHT (data are mean ± SEM, $n = 3$). **E,** Exogenous expression of wild-type DIS3L expression restores MYC-induced cell death by treatment with 60 nmol/L 4-OHT for 24 hours in cells with endogenous DIS3L depletion. MYC-ER HMEC cells were engineered with control- or shRNA-resistant-DIS3L cDNA and treated as in **D**; (data are mean ± SEM, $n = 3$). **F–G,** MYC induces elevated RNA decay that requires DIS3L. MYC-ER HMECs with control or DIS3L shRNA [(**F**), (**G**) respectively] were labeled with EU for 1 hour ±60 nmol/L 4-OHT to induce MYC-ER. EU was washed out for the indicated "chase" time, and cellular EU intensity was measured via microscopy. Linear regression shows that MYC induces RNA decay (**F**) and this effect is suppressed by DIS3L depletion (**G**; $n > 100$ cells per group). **H,** MYC-induced expression of abundant RNAs is restrained by the DIS3L ribonuclease. Oncogenic MYC was induced in MYC-ER HMECs with 60 nmol/L 4-OHT for 24 hours with control or DIS3L shRNA, and gene expression measured by RNAseq (ribo-depleted RNA). Genes with FPKM > 1 were divided into 10 deciles based on mean RNA expression across all samples (highest decile in red on left). For each decile, plot shows mean changes in gene expression induced by MYC in DIS3L-depleted state vs. control state. MYC-induces a greater change after DIS3L-depletion in the genes in the top decile (high abundance RNAs) compared to the bottom decile (low abundance RNAs; 1 = HIGHEST, 10 = LOWEST). **I,** MYC-induced expression of top 500 abundant RNAs is restrained by the DIS3L ribonuclease. RNAseq data from (**H**) for the 500 most abundant RNAs is shown, with the effect of MYC in control shRNA cells plotted on the x-axis, and the effect of MYC in DIS3L-shRNA cells plotted on the y-axis. Significance was analyzed by binomial test for **B**; by two-tailed, unpaired Student *t* test for **D**,**E**, and **H**; and slopes for **F** and **G** were compared using GraphPad Prism's simple linear regression. *P, < 0.05; **, $P < 0.01$; ***, $P < 0.001$.

scaffold components (e.g., EXOSC6, EXOSC8) and the catalytic subunit (DIS3L) of the cytoplasmic exosome were enriched in the primary screen (Supplementary Fig. S1K; Supplementary Tables S1 and S2). Given that the original genetic screen was performed with a shallow library (mean of 2.31 shRNAs/gene), we sought to test whether DIS3L and other exosome components were on-target hits using several orthogonal approaches. In individual shRNA validation experiments, multiple shRNAs targeting these subunits suppressed MYC-induced cell death (Fig. 2D; Supplementary Fig. S2A–S2H). Inducible expression of shRNA-resistant DIS3L restored MYC-induced cell death (Fig. 2E; Supplementary Fig. S2D), thereby validating that the phenotype is an RNAi on-target effect.

Given that the exosome scaffold components are shared between the nuclear and cytoplasmic exosome complexes (53–55), we investigated whether the nuclear exosome also mediates MYC-induced cell death. Interestingly, knockdown of the nuclear exosome exonuclease (DIS3) did not impact MYC-induced cell death (Supplementary Fig. S2I and S2J), even though significant RNA turnover is known to occur in the nucleus (56). This suggests that cytoplasmic, rather than nuclear, RNA degradation by the exosome is a critical mediator of MYC-induced cell death. To test whether DIS3L, which is localized exclusively in the cytoplasm, impacts MYC-induced increase in RNA decay, we performed EU pulse-chase experiments with and without knockdown of DIS3L. Depletion of DIS3L suppressed the MYC-induced increase in RNA decay rate (Fig. 2F and G) without affecting MYC-induced increase in RNA synthesis (Supplementary Fig. S2K). This indicates that cytoplasmic RNA is the major source of RNA whose degradation is impacted by MYC hyperactivation.

Collectively, these data suggested that MYC-induced cell death is, in part, dependent on cytoplasmic RNA decay (and potentially downstream ribonucleotide catabolites) that is mediated by the DIS3L ribonuclease. However, because mRNA decay can also be induced by apoptosis (57), we evaluated an alternative hypothesis that MYC-induced RNA decay is a downstream consequence of MYC-induced apoptosis. To test this, we evaluated the timing of both MYC-induced RNA decay and MYC-induced cell death. Notably, we found that while MYC-induced RNA decay and ribonucleotide catabolism occurs within 4 hours of MYC hyperactivation (Figs. 1B-D and 1H), MYC-induced cell death is observed long after this time point (24 hours; and Fig. 2D). To verify this timing, we measured MYC-induced apoptosis by annexin V, caspase 3/7 assay, and time-lapse imaging. We did not find significant induction of apoptosis within 4 hours post-MYC-hyperactivation (Supplementary Fig. S3A–S3D) when RNA decay was observed. These observations indicated that MYC-induced RNA decay and ribonucleotide catabolism precede MYC-induced cell death. Moreover, ectopic expression of BCL2 [which inhibits MYC-driven cell death (58, 59)] did not alter MYC-induced RNA decay (Supplementary Fig. S3E-F). These data are consistent with the hypothesis that MYC-induced RNA decay is not a consequence of cell death but instead may contribute to MYC-induced apoptosis.

Given our observation that cytoplasmic RNA decay may contribute to MYC-induced cell death, we sought to investigate the pools of RNAs that might be dysregulated by MYC hyperactivation specifically when DIS3L is impaired. In particular, we hypothesized that such pools of RNA may contribute to the downstream accumulation of RNA degradation products and ribonucleotide catabolites that are observed when MYC is aberrantly activated (Fig. 1). Given that rRNA turnover rates (half-life ~2 to 4 days) are significantly less than that of mRNA (average half-life ~9 hours; refs. 60–63), we sequenced rRNA-depleted RNA. We compared MYC-induced changes in RNA expression levels in cells with and without DIS3L knockdown. Strikingly, when we compared the MYC inducibility of RNAs in each decile of steady-state abundance, the most abundant transcripts in the baseline state were also the most highly induced by MYC in the DIS3L-depleted state but not in the control-shRNA state (Fig. 2H; Supplementary Fig. S3G). In addition to coding mRNAs, these high abundance transcripts included many small RNAs like snoRNAs and microRNAs (Fig. 2I). In contrast, MYC-induced expression changes for lowly expressed transcripts were less impacted by knockdown of DIS3L (Fig. 2H; Supplementary Fig. S3G). This suggests that the ability of MYC to induce RNAs that are already highly abundant is counterbalanced by DIS3L-mediated degradation. It also suggests that this highly abundant pool of RNAs may be a prominent source of ribonucleotide catabolites and oncogenic stress in the context of MYC hyperactivation. Notably, MYC hyperactivation had only modest or no effect (0%–20% change) on expression levels of the RNA exosome itself (including DIS3L; Supplementary Fig. S3H), suggesting that MYC-induced RNA decay likely does not occur through direct upregulation of the RNA exosome.

Taken together, these results suggest that MYC-induced RNA synthesis is followed by widespread cytoplasmic RNA decay mediated by DIS3L that maintains homeostasis of highly expressed RNAs. This also supports the hypothesis that MYC-induced RNA decay produces a collateral effect of increased accumulation of downstream ribonucleotide catabolites, ROS, and cell death (explored in more detail below).

Tumor-Derived Mutations in *DIS3L* Mitigate MYC-Induced Oncogenic Stress

Oncogenic MYC activity leads to apoptotic signaling that serves as a barrier to cancer progression in the absence of cooperating mutations (8, 9). Our discovery that loss of DIS3L function can suppress MYC-induced cell death raised the hypothesis that DIS3L may be a tumor suppressor. Thus, we evaluated whether DIS3L function may be compromised in human cancer. We noted that somatic mutations occur in the *DIS3L* locus in breast cancer and other malignancies with a pan-cancer frequency of 1.4% in 10,953 patients from cBioPortal (http://www.cbioportal.org; Supplementary Fig S4A; ref. 64). To assess which mutations, if any, are likely to impact DIS3L function, we performed an evolutionary analysis on *DIS3L* somatic mutations from pan-cancer collections. Evolutionary action (EA) predicts the effect of genotype perturbations on protein fitness and function (65). Evolutionary trace (ET) scores that indicate the functional role of each genotype position were aligned and mapped onto the crystal structure of DIS3L's structural and functional homolog, *Saccharomyces cerevisiae* Dis3 (Fig. 3A; ref. 66). EA analysis revealed a strong enrichment of deleterious mutations (EA score > 60) within the RNA-interacting domains including the exonuclease domain (Supplementary Fig. S4B; Supplementary

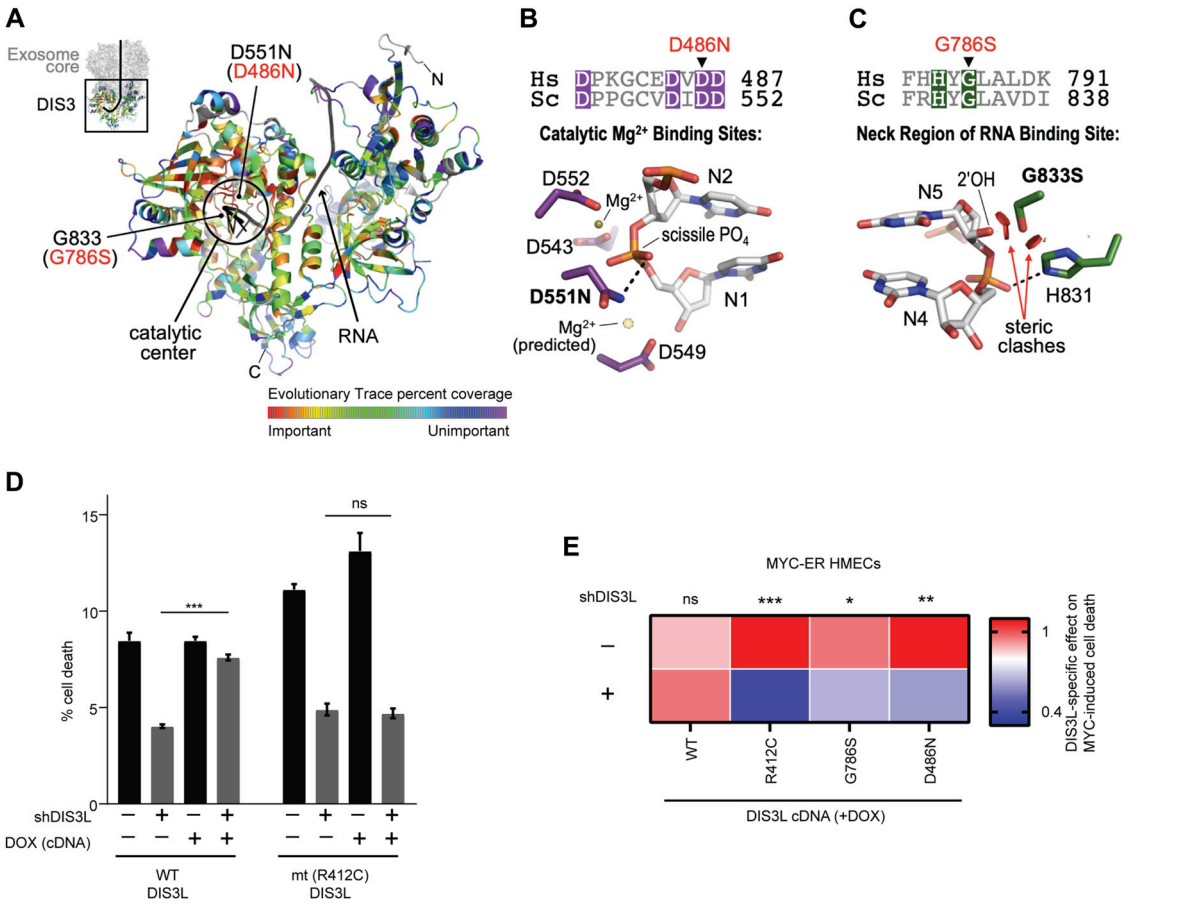

Figure 3. Tumor-derived mutations in *DIS3L* mitigate MYC-induced cell death. **A,** Deleterious tumor mutations in *DIS3L* occur in RNA interacting domains including the exonuclease domain. ET scores, which predict the impact of amino acids on protein function, were mapped onto the structure of the functional DIS3L homologue, *S. cerevisiae* Dis3 (PDB ID 4IFD), with high ET scores clustering in RNA interacting motifs and the catalytic center. Color map of ET coverage displays the estimated importance of each amino acid residue in the DIS3L protein, ranging from red (most important) to purple (least important). Demarcated are RNA (black) and tumor-derived mutations occurring in the catalytic core, with positions annotated for *S. cerevisiae* Dis3 (black) and human DIS3L (red). **B–C,** Tumor-derived mutations are predicted to interfere with functions required for DIS3L activity, including catalytic metal and RNA-binding sites. Amino acid sequence alignments of *H. sapiens* DIS3L (Hs) and *S. cerevisiae* Dis3 (Sc) highlight the conservation of catalytic core residues of DIS3L- D486 and G786. Corresponding ribbon diagrams show the predicted impact of equivalent *S. cerevisiae* Dis3 mutations D551N (D486N in *H. sapiens*; **B**) and G833S (G786S in *H. sapiens*; **C**). **B,** Dis3 D551 is one of four conserved aspartate residues that, along with D543, D549, and D552, form electrostatic interactions with the incoming RNA near the scissile phosphate (PO_4). D551 also coordinates the predicted second divalent metal ion (Mg^{2+} (predicted)) at the catalytic center necessary for Dis3 two-metal-ion catalysis (67). **C,** Dis3 G833 lies at a structural position along a narrow stretch of the RNA channel known as the neck region. Structural modeling of Dis3 G833S results in steric clashes with neighboring H831 and a nearby 2'-hydroxyl of the threaded RNA, likely resulting in indirect and direct RNA binding defects, respectively. Pairwise overlap of van der Waals radii (steric clashes) are displayed as red disks. Hydrogen bonds between Dis3 and RNA are shown as black dotted lines. **D,** Tumor-derived R412C mutation in DIS3L compromises MYC-induced cell death. MYC-ER HMECs were engineered with control- or DIS3L-shRNA and a doxycycline-inducible wild-type or mutant DIS3L cDNA that is resistant to DIS3L shRNA. Bar graph represent MYC-induced cell death upon treatment with 60 nmol/L 4-OHT for 24 hours in control- and DIS3L-depleted state with or without cDNA expression. Wild-type DIS3L cDNA, but not the R412C mutant DIS3L, restored MYC-induced cell death in the presence of DIS3L-shRNA (data are mean ± SEM, $n = 3$). **E,** Tumor-derived mutations in DIS3L compromise MYC-induced cell death where cells were incubated ±60 nmol/L 4-OHT to induce MYC-ER. Heatmap of MYC-induced cell death upon overexpression of wild-type or indicated mutant DIS3L cDNA (±DIS3L shRNA). In contrast to wild-type cDNA, DIS3L mutants R412C, G786, and D486N did not restore MYC-induced cell death. Data are normalized to cell death in MYC-induced state with control shRNA. Significance was analyzed by two-tailed, unpaired Student *t* test for **D** and **E**. *, $P < 0.05$; **, P, <0.01; ***; P, < 0.001.

Table S3; ref. 66). Notably, several mutations with high EA scores were recurrent across cancers (Supplementary Fig. S4A and S4B) including mutations within the exonuclease domain, suggesting that the ability of the cytoplasmic exosome to degrade RNA may be compromised in multiple cancer types. To better understand the impact of cancer-derived mutations in *DIS3L*, we analyzed the residues that are conserved in *S. cerevisiae* Dis3 and predicted their impact on DIS3L functionality. In general, mutations in *DIS3L* fall into five categories- (i) protein misfolding/instability (e.g., V347E), (ii) exosome core interaction defect (e.g., R104Q), (iii) direct and indirect RNA-binding defects (Fig. 3B and C; e.g., D486N and G786S), (iv) incomplete DIS3L expression (e.g., R262*), and (v) unexplained defects (e.g., R412C). Overall, these structure-based predictions suggest that DIS3L function may be compromised in *DIS3L*-mutated human cancer.

To test the functional consequence of these tumor-derived DIS3L mutations, we evaluated three DIS3L mutations with a high EA score (>60), for their impact on MYC-induced cell death. To this end, endogenous *DIS3L* was knocked down

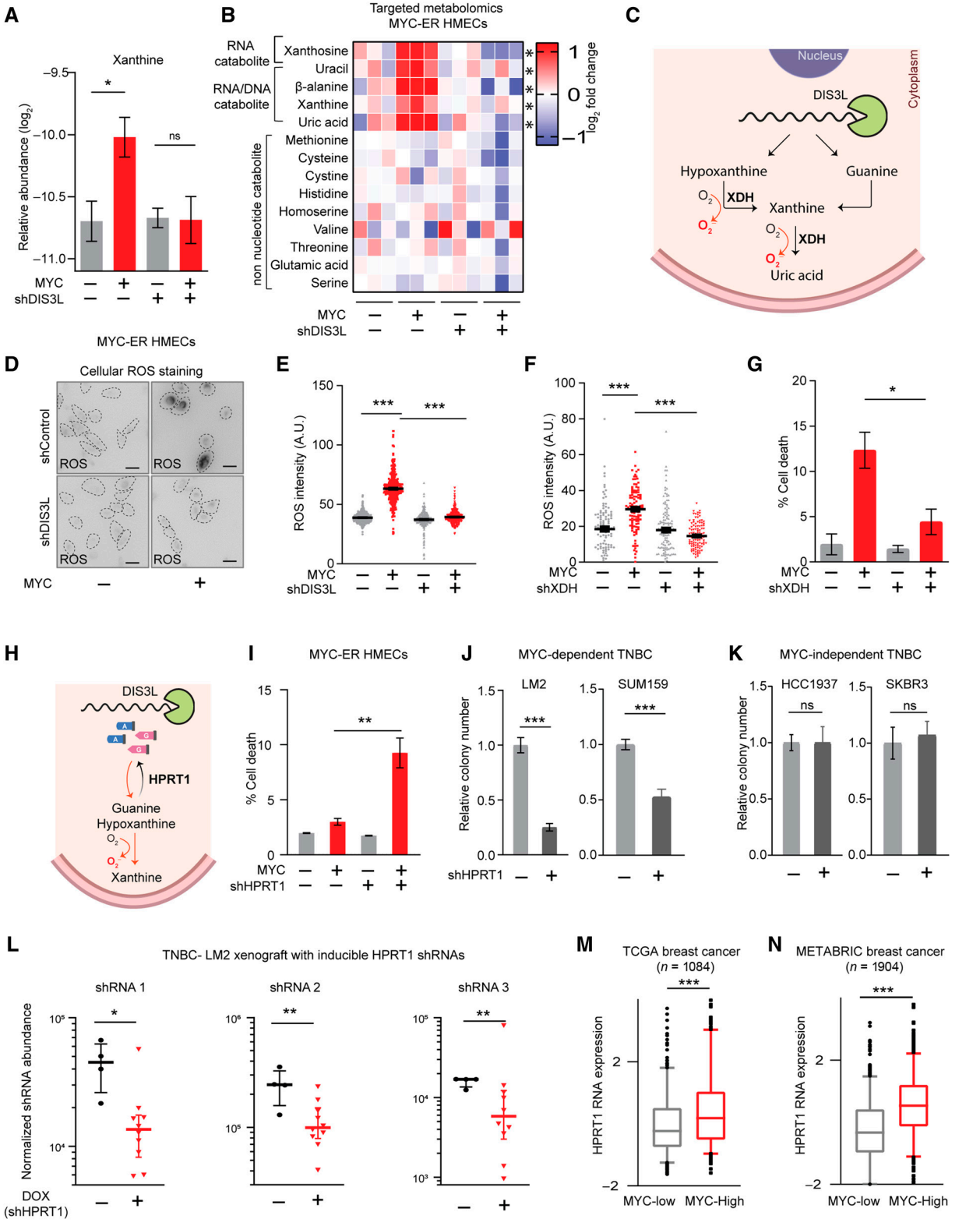

Figure 4. Oncogenic MYC induces cell death through DIS3L-mediated ribonucleotide catabolism and increases dependency on ribonucleotide salvage and HPRT1. **A** and **B,** DIS3L is required for oncogenic MYC to induce RNA catabolites. MYC-ER was induced for 4 hours treatment with 60 nmol/L 4-OHT in HMECs expressing control- or DIS3L-shRNA, and cells were evaluated via targeted metabolomics for catabolites specific for RNA degradation [shown in top row of (**B**), catabolites specific for RNA or DNA degradation (**A**) and rows 2-5 of (**B**)] or metabolites unrelated to RNA degradation [data are mean ± SEM, $n = 3$ for (**A**) and log2 fold change in catabolites in MYC-hyperactivated conditions relative to MYC-normal in respective genotypes for (**B**)]. (*continued on following page*)

in MYC-ER HMECs with an shRNA targeting the 3′UTR of *DIS3L*, and *DIS3L* wild-type or mutant cDNAs were expressed in these cells. Notably, all three mutations (R412C, D486N, and G786S) impaired MYC-induced cell death (Fig. 3D and E). In addition, mutation of one of the DIS3L catalytic residues (D486; refs. 53, 54) abrogated MYC-induced cell death (Fig. 3E), strongly suggesting that RNA degradation by the exosome is required, in part, for MYC-induced cell death.

These data suggest that the ability of DIS3L to degrade RNA and contribute to MYC-induced cell death may be partially compromised in human cancers. However, we noted that the frequency of these somatic mutations were relatively low (1.4% pan cancer). Thus, we evaluated whether the *DIS3L* locus is compromised by additional mechanisms. Notably, we found that ~30% of breast cancers harbor shallow genomic deletions in *DIS3L* that associate with lower *DIS3L* mRNA levels (Supplementary Fig. S4C–S4E). Importantly, *DIS3L* deletions also associate with *MYC* amplification (Supplementary Fig. S4D), consistent with the hypothesis that *MYC*-amplified tumors may select for reduced DIS3L function. To further explore this possibility, we analyzed *DIS3L* mRNA and *MYC* copy number in cohorts of breast tumors. Notably, we found that *DIS3L* mRNA is significantly downregulated in *MYC*-amplified tumors compared to MYC-nonamplified tumors (Supplementary Fig. S4F). These data suggest DIS3L downregulation is a common feature of MYC-driven breast tumors. More broadly, these data suggest that DIS3L-mediated RNA decay is required for MYC-induced cell death, at least in some contexts, and that this function of DIS3L may be partially compromised in human cancer. Further studies are needed to determine whether RNA degradation is compromised by other mechanisms (in addition to *DIS3L* mutation and expression) in MYC-driven malignancies.

DIS3L Mediates Accumulation of Ribonucleotide Catabolites and Cytotoxic ROS Due to MYC Hyperactivation

The genetic data and mutational analysis presented above indicate that DIS3L mediates an increase in RNA decay and cell death in the context of MYC hyperactivation. Notably, the process of ribonucleotide catabolism produces cytotoxic ROS, several catabolites, and intermediates (e.g., xanthine, uric acid; example diagram in Fig. 1E; refs. 48–50). Given our data that MYC upregulates ribonucleotide catabolites (Fig. 1), we hypothesized that this increase is the consequence of RNA decay mediated by the cytoplasmic exosome (and DIS3L). Indeed, depletion of DIS3L alone significantly suppressed MYC-induced levels of both purine and pyrimidine ribonucleotide catabolites, suggesting that DIS3L-mediated RNA decay is critical for aberrant accumulation of these catabolites (Fig. 4A and B). Notably, knockdown of DIS3L did not significantly lower the effect of MYC-induction on the expression of genes implicated in ribonucleotide catabolism and synthesis or the genes known to play antiapoptotic roles (Supplementary Fig. S4G, S4H, and S5A). This supports the model that DIS3L regulates catabolite levels via widespread degradation of RNA rather than regulation of specific gene products.

MYC hyperactivation leads to increased ROS in many cell and cancer types (68–70). ROS accumulation has been proposed to be a major oncogenic stress in the context of MYC oncogenesis and is a target of current therapeutic efforts against MYC-driven cancers (40). However, the mechanisms underlying MYC-induced ROS generation have remained unclear. Prior observations have suggested that MYC-induced ROS may arise from several mechanisms including induction of p53 target genes, induction of a MYC-target gene ODC, biochemical imbalances in mitochondrial metabolism, overexpression of NADPH oxidases, and increased oxygen consumption (68–70). Because ribonucleotide catabolism produces ROS at several steps, we hypothesized that RNA decay and ribonucleotide catabolism may be a major source of MYC-induced ROS (Fig. 4C). Similar to other cell types, MYC hyperactivation in HMECs led to robust ROS accumulation [Fig. 4D (top) panels, quantification in Fig. 4E]. Depletion of DIS3L completely suppressed MYC-induced ROS but did not impact baseline levels of ROS (Fig. 4D and E), suggesting that RNA decay is required for ROS generation in response to MYC hyperactivation.

To determine if MYC-induced ROS is dependent on downstream ribonucleotide catabolism, we measured ROS and subsequent cell death in the context of depletion of xanthine dehydrogenase (XDH), an enzyme that functions in the last steps of purine catabolism. XDH converts hypoxanthine into xanthine and uric acid and at both catalytic steps reduced XDH reacts with molecular oxygen (O_2) to produce superoxides (O_2^-; ref. 71). Similar to DIS3L depletion, reduction in XDH levels via shRNA mitigated MYC-induced ROS and cell death (Fig. 4F and G). Similarly, XDH-inhibitor allopu-

Figure 4. ***(Continued)*** **C,** Schematic shows the XDH-dependent steps in terminal purine ribonucleotide catabolism that produce ROS. **D** and **E,** DIS3L is required for oncogenic MYC to induce ROS. MYC-ER was induced with 60 nmol/L 4-OHT for 16 hours in HMECs expressing control- or DIS3L-shRNA, and cells were evaluated for ROS via CellROX. Representative images of MYC-induced cellular ROS (shown by black pseudocolor, top right picture), which is suppressed by DIS3L depletion (bottom right). Scale bar is 40 μm. Associated quantification in (**E**; $n > 100$ cells per group). **F,** XDH is required for oncogenic MYC to induce ROS. MYC-ER was induced for 16 hours with 60 nmol/L 4-OHT in HMECs expressing control- or XDH-shRNA, and cells were evaluated for ROS via CellROX ($n > 100$ cells per group). **G,** XDH is required for MYC-induced cell death. MYC-ER was induced for 24 hours with 60 nmol/L 4-OHT in HMECs expressing control- or XDH-shRNA, and cells were evaluated for cell death (measured via PI incorporation). **H,** Schematic showing the salvage of hypoxanthine and guanine by HPRT1. **I,** Oncogenic MYC is synthetic lethal with HPRT1 inhibition. MYC-ER was induced with 4 nmol/L 4-OHT in HMECs with and without HPRT1 depletion. Cell death was measured via PI incorporation (data are mean ± SEM, $n = 3$). **J–K,** MYC-dependent breast cancer cell lines are dependent on HPRT1. MYC dependent (**J**) or MYC independent (**K**) breast cancer cells were engineered with or without HPRT1 depletion and measured for anchorage-independent proliferation (data are mean ± SEM, $n = 3$–8). **L**, HPRT1 depletion impairs progression of established MYC-driven TNBC xenografts. MDA-MB-231 LM2 xenografts cells were transduced with lentivirus encoding three independent doxycycline-inducible HPRT1-shRNAs (or control shRNAs). After tumor formation, animals were randomized ±DOX for 2 weeks. shRNA abundance was quantified using next-generation sequencing. Dot plots show the abundance of *HPRT1* shRNA in tumor xenografts (−DOX, $n = 4$; +DOX, $n = 10$). **M** and **N,** *HPRT1* RNA expression is higher in MYC-high breast tumors vs. MYC-low breast tumors in TCGA cohort (**M**) and METABRIC cohort (**N**). MYC-high or low tumors were defined as the top or bottom tertile of MYC RNA expression. Significance was analyzed by two-tailed, unpaired Student *t* test for **A**, **B**, **E**–**G**, and **I**–**N**. ROUT ($Q = 1\%$) outlier analysis was done for the **L** right most (relating to *HPRT1* shRNA3). *, $P < 0.05$; **, $P < 0.01$; ***, $P < 0.001$.

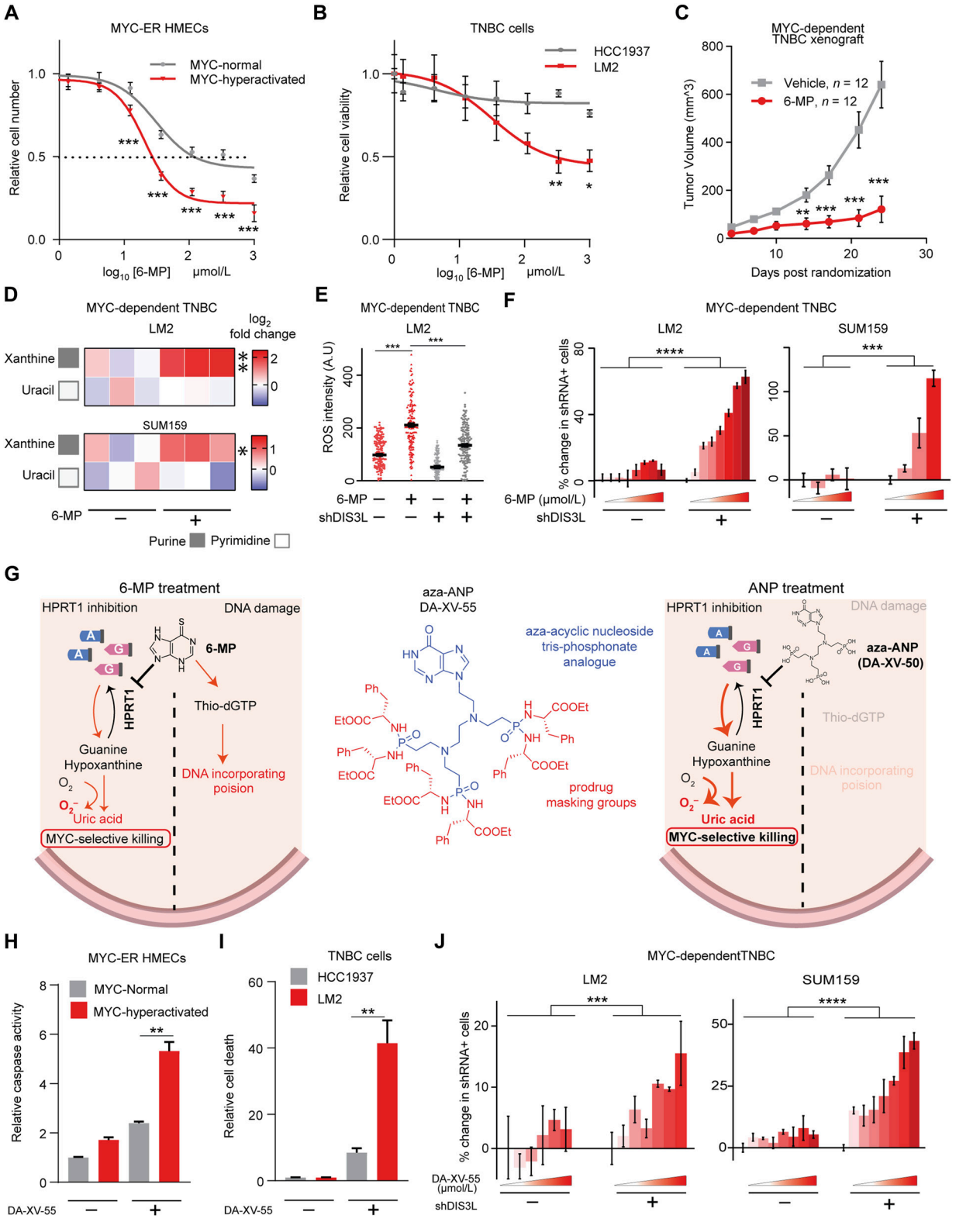

Figure 5. Therapeutic inhibition of HPRT1-mediated ribonucleotide salvage kills MYC-driven breast cancer cells through exacerbating RCS. **A,** MYC hyperactivation enhances sensitivity to 6-MP. MYC-inducible HMECs were exposed to increasing doses of 6-MP for 24 hours ±MYC hyperactivation with 12 nmol/L 4-OHT (data are mean ± SEM, $n = 3$). **B,** MYC-hyperactive TNBC cells exhibit increased sensitivity to 6-MP. MYC-hyperactive TNBC cells (LM2) or MYC-normal TNBC cells (HCC1937) were exposed to increasing doses of 6-MP for 24 hours and measured for cell viability. **C,** 6-MP impairs MYC-hyperactive tumor progression. After transplantation, LM2 xenografts were randomized ±12.5 mg/kg 6-MP and measured for tumor volume ($n = 12$ mice per group). **D,** 6-MP induces purine catabolites but not pyrimidine catabolites in MYC-dependent (*continued on following page*)

rinol suppressed MYC-induced apoptosis (Supplementary Fig. S5B). To directly test if an increase in these RNA catabolites may contribute to cell death, we treated *MYC*-amplified TNBC cells with exogenous xanthosine, which is converted to cytotoxic catabolites xanthine and uric acid in cells, and also increases the production of toxic superoxides (O_2^-) in the process. Consistent with the model that ribonucleotide catabolite accumulation gives rise to oncogenic stress and cell death, xanthosine treatment led to growth inhibition and apoptosis in TNBC cells, and increased ROS accumulation and MYC-induced cell death in MYC-ER HMECs (Supplementary Fig. S5C–S5F). Collectively, these data support the hypothesis that aberrant MYC hyperactivation leads to enhanced RNA decay, ribonucleotide catabolism, and ROS generation that contribute to MYC-induced cell death and may serve as an oncogenic stress that limits tumor progression.

Oncogenic MYC Increases Tumor Cell Dependency on Ribonucleotide Salvage

The results above indicate that MYC-hyperactive cancers may harbor increased levels of ribonucleotide catabolites and ROS, and thus depend on mechanisms to mitigate accumulation of such potentially toxic catabolites (model in Fig. 4H). During normal homeostasis, the accumulation of ribonucleotide catabolites is primarily counterbalanced by nucleotide salvage pathways, especially via the purine salvage enzyme HPRT1, which converts hypoxanthine and guanine into IMP and GMP, respectively (50). Therefore, we hypothesized that MYC hyperactivation may lead to a heightened dependency on HPRT1 in a manner that depends on elevated RNA decay. To evaluate this hypothesis, we first tested whether MYC induction causes sensitivity to HPRT1 inhibition. In this experimental context, we lowered the MYC-ER induction (using reduced levels of 4-OHT) in order to observe potential MYC-synthetic lethality. Indeed, HPRT1-depletion with multiple shRNAs was synthetic lethal with MYC hyperactivation in HMECs (Fig. 4I; Supplementary Fig. S5G and S5H). HPRT1-depletion also impaired anchorage-independent proliferation of MYC-dependent breast cancer cells in contrast to MYC-independent breast cancer cell lines (Fig. 4J and K). Likewise, doxycycline-inducible shRNAs targeting HPRT1 significantly impaired progression of MYC-hyperactive breast cancer xenografts, as measured by pooled *in vivo* tumor competition assays (data for three independent shRNAs in Fig. 4L). In contrast, shRNAs targeting *DIS3L* significantly enhanced progression of MYC-hyperactive breast cancer xenografts (Supplementary Fig. S5I). These data suggest that MYC-hyperactive breast cancer cells harbor an enhanced dependency on HPRT1. We hypothesized that in the context of human breast cancers, MYC-hyperactive tumor cells exhibit increased reliance on HPRT1 to mitigate stress from increased RNA catabolism and thus may select for higher HPRT1 levels during tumorigenesis. Consistent with this hypothesis, MYC-high tumors in both The Cancer Genome Atlas (TCGA) and METABRIC cohorts had a higher expression of *HPRT1* (Fig. 4M and N).

Therapeutic Inhibition of HPRT1 Kills MYC-Driven Breast Cancer Cells through a Mechanism That Depends on RNA Decay but Is Independent of DNA Incorporation

The observations above suggest MYC-hyperactive cancers may be sensitive to inhibition of HPRT1. Notably, 6-mercaptopurine (6-MP) is an HPRT1 competitive inhibitor that has been studied and used for decades as an anticancer agent and immunosuppressant (72, 73) in the clinic. However, the core mechanism proposed for the ability of 6-MP to kill cancer cells and suppress the immune system is as a DNA incorporating poison, not as an HPRT1 antagonist. More specifically, studies suggest cancer and immune toxicities are induced by 6-MP because it is converted by HPRT1 into thio-dGTP, which in turn is a substrate for DNA polymerase that causes cytotoxicity once incorporated into DNA (72). However, our observations that genetic perturbation of HPRT1-function alone may selectively kill MYC-driven cancers raised the provocative hypothesis that 6-MP may have anticancer activity through a second unanticipated mechanism: exacerbation of purine catabolism in MYC-hyperactive cells, resulting in increased production of cytotoxic ribonucleotide catabolites and ROS. To evaluate this hypothesis, we first investigated whether oncogenic MYC increases sensitivity to 6-MP, and whether 6-MP enhanced purine ribonucleotide catabolism in MYC-hyperactive breast cancer cells. Notably, in MYC-ER HMECs, MYC-induction significantly increased sensitivity to 6-MP (decrease

Figure 5. ***(Continued)*** TNBC cells. LM2 or SUM159 cells were treated with 100 μmol/L 6-MP for 12 hours and measured for xanthine and uracil by targeted metabolomics. Heatmap shows log2 fold change in metabolites relative to the control treatment state ($n = 3$). **E,** 6-MP induces ROS in TNBC cells in a DIS3L-dependent manner. LM2 cells engineered with control- or DIS3L-shRNA were treated with 50 μmol/L 6-MP for 24 hours and measured for ROS by CellROX assay ($n > 100$ cells per group). **F,** Loss of DIS3L confers resistance to 6-MP in MYC-hyperactive TNBC cells. LM2 (left) or SUM159 (right) cells were engineered with a doxycycline-inducible control- or DIS3L-shRNA that also expresses RFP. Each population was mixed (separately) with non-RFP LM2 or SUM159, treated with increasing doses of 6-MP, and fitness of shRNA-expressing cells was measured over time as RFP-positive population (data are mean ± SEM, $n = 3$). **G,** left, Schematic of proposed 6-MP modes of action. 6-MP may kill cancer cells through two distinct mechanisms: (i) As an HPRT1 antagonist (left side), 6-MP may prevent nucleotide salvage and enhance MYC-selective cancer cell killing; (ii) 6-MP is converted into thio-dGTP (right side), which serves as a DNA incorporating poison and may kill cells in a manner independent of MYC. **G**, middle, Structure of aza-ANP DA-XV-55. DA-XV-55 is an HPRT1 antagonist that cannot be incorporated into DNA. The modified nucleotide moiety (marked in blue) is the active species, i.e. inhibitor of HPRT1 *in vitro* (74) while the masking prodrug moieties (marked in red) enable cell permeability. **G**, right, Parent aza-ANP DA-XV-50 may kill cancer cells selectively through inhibiting HPRT1 function. DA-XV-50 inhibits HPRT1 and may impair nucleotide salvage (left side), but it cannot be metabolized into a DNA incorporating poison (in contrast to 6-MP).**H,** MYC-hyperactivation enhances DA-XV-55-induced cell death. MYC-ER HMECs were treated with vehicle or 10 μmol/L DA-XV-55 in absence/presence of MYC-hyperactivation with 12 nmol/L 4-OHT and measured for caspase 3/7 activity (data are mean ± SEM, $n = 3$).**I,**MYC-hyperactive TNBC cells exhibit increased sensitivity to DA-XV-55. MYC-hyperactive TNBC cells (LM2) or MYC-normal TNBC cells (HCC1937) were exposed to 10 μmol/L DA-XV-55 and measured for cell viability (data are mean ± s.e.m., $n = 3$).**J,** Loss of DIS3L confers resistance to DA-XV-55 in MYC-hyperactive TNBC cells. LM2 (left) or SUM159 (right) cells were engineered with a doxycycline-inducible control- or DIS3L-shRNA that also expresses RFP. Each population was mixed (separately) with non-RFP LM2 or SUM159, treated with increasing doses of DA-XV-55, and fitness of shRNA-expressing cells was measured over time as RFP-positive population (data are mean ± SEM, $n = 3$). Significance was analyzed by two-tailed, unpaired Student *t* test for **A**–**E**, **H**, and **I**. Fold shift in the dose–response curve was tested using nonlinear regression for **F** and **J**, *, $P < 0.05$; **, $P < 0.01$; ***, $P < 0.001$.

in GI50 by nine-fold) (Fig. 5A), suggesting that MYC hyperactivation is sufficient to drive sensitivity to 6-MP. Similarly, MYC-dependent cancer cell lines were more sensitive to 6-MP than MYC-independent models (Fig. 5B; Supplementary Fig. S6A–S6D). Finally, single-agent 6-MP impaired progression of MYC-driven breast cancer xenografts (Fig. 5C). These data suggest that MYC hyperactivation is at least one mechanism that drives sensitivity to 6-MP in human cancers.

These observations raise the hypothesis that 6-MP anticancer activity may depend, in part, on enhanced ribonucleotide (purine) catabolism. Notably, 6-MP caused an increase in xanthine (Fig.5D) and uric acid (Supplementary Fig. S6E), consistent with impaired HPRT1-mediated salvage, but did not impact accumulation of uracil, which is a pyrimidine catabolite independent of HPRT1 activity (Fig. 5D). This was accompanied by increased levels of ROS (Fig. 5E), consistent with impaired purine salvage and enhanced purine catabolism. Importantly, shRNA-depletion of DIS3L abrogated 6-MP-induced ROS (Fig. 5E) and conferred resistance to 6-MP (Fig. 5F), indicating that partially decreased RNA decay is sufficient to lower the flux through this catabolic pathway and enhance cell survival in the context of MYC hyperactivation. Further supporting this model, depletion of the enzyme XDH that catalyzes hypoxanthine and xanthine and produces ROS conferred resistance to 6-MP-driven cell death in MYC-hyperactivated conditions (Supplementary Fig. S6F). Overall, these data suggest that RNA decay and ribonucleotide catabolism by XDH are required for 6-MP induced cancer cell death in MYC-hyperactivated settings. As an alternative hypothesis, we tested if inhibiting HPRT1 may also cause cytotoxicity through depletion of the purine nucleotides. Notably, the levels of guanine and GMP were not impacted by 6-MP treatment (Supplementary Fig. S6G), suggesting that inhibition of ribonucleotide salvage enhances terminal purine ribonucleotide catabolism and may primarily cause toxicity by accumulation of ribonucleotide catabolites. Consistent with this hypothesis, supplementation with IMP had a minor effect and was not able to fully rescue cell viability in MYC-dependent LM2 cells. In addition, supplementation with GMP had no effect on 6-MP-induced cytotoxicity (Supplementary Fig. S6H). Likewise, a second MYC-high TNBC cell line (SUM159) did not show significant rescue of 6-MP induced cytotoxicity by IMP or GMP supplementation (Supplementary Fig. S6I). Taken together, these results indicate that 6-MP may impair the survival and progression of MYC-driven cancers through an unanticipated mechanism of action independent of DNA incorporation.

While 6-MP is effective in some cancers (72), its efficacy has been largely hampered by dose-limiting toxicities in normal tissues, and these toxicities have been attributed to the DNA-incorporation properties of 6-MP metabolites [Fig. 5G (left panel)]. Our data suggest that sensitivity to 6-MP in MYC-driven cancers may be dependent on inhibition of purine salvage as opposed to DNA incorporation/DNA damage. Thus, we were interested in a pharmacologic strategy that specifically targets purine salvage without incorporating into DNA, thus avoiding potential patient toxicities associated with this mechanism of action (Fig. 5G, model contrasted in left and right panels). To test this, we evaluated acyclic nucleoside phosphonate (ANP) DA-XV-50, a potent competitive inhibitor of human HPRT1 (*i.e.*, *Ki* = 10 nmol/L; ref. (74)). For these studies, a prodrug form of DA-XV-50, identified as DA-XV-55 [Fig. 5G (middle) panel], was synthesized to enhance cell permeability. Once inside the cell, the lipophilic attachments are cleaved by endogenous esterases to release DA-XV-50, which then inhibits HPRT1. Because of its stable chemical structure and bulk, DA-XV-50 is incapable of being a substrate for DNA polymerase and therefore cannot incorporate into DNA [Fig. 5G (right) panel]. In MYC-ER HMECs, we tested if DA-XV-55 is MYC-synthetic lethal. Notably, DA-XV-55 treatment resulted in a greater increase in caspase-3 and -7 activity in MYC-hyperactivated cells compared to MYC-normal cells (Fig. 5H). Likewise, DA-XV-55 induced greater cell death in MYC-dependent breast cancer cells (LM2) compared to MYC-independent breast cancer cells (HCC1937; Fig. 5I). To test if DA-XV-55 driven cell death is dependent on DIS3L-mediated RNA decay, we performed a competition assay in MYC-dependent breast cancer cells (SUM159 and LM2) with DIS3L or control shRNA. In line with our hypothesis, depletion of DIS3L conferred dose-dependent resistance to DA-XV-55 in MYC-dependent breast cancer cells (Fig. 5J). Overall, these results suggest that the HPRT1 inhibitor DA-XV-55, which cannot incorporate into DNA, is synthetic lethal with MYC hyperactivation and drives cell death through DIS3L-mediated RNA decay. Because the pharmacokinetic properties of DA-XV-55 prevent *in vivo* testing, additional medicinal chemistry and preclinical studies will be required to evaluate this hypothesis in the setting of MYC-driven tumor progression. More broadly, these results provoke the hypothesis that pharmacologic strategies to inhibit HPRT1 and exacerbate ribonucleotide catabolism (but preventing DNA incorporation) may be a new approach to ameliorating MYC-driven cancers.

DISCUSSION

Hyperactivation of MYC is one of the most common events in human cancer and thus there have been major efforts to delineate how this oncogene drives tumorigenesis and to subvert these mechanisms therapeutically. Particular attention has been paid to how MYC hyperactivation imposes a metabolic stress on cancer cells. Prior studies have shown that this stress is, in part, due to the biosynthetic demand of increased production of macromolecules (e.g., nucleic acids and protein) necessary to sustain cell proliferation, survival, and other protumorigenic programs (20–22, 25, 26, 28, 29). In contrast, little attention has been given to the catabolic pathways that counterbalance the oncogenic programs driving widespread macromolecular synthesis (23, 24, 30). Herein, we have discovered that oncogenic activation of MYC induces cell death through a new mechanism: widespread elevation in RNA decay and downstream accumulation of toxic ribonucleotide catabolites and associated ROS. Moreover, we show that this new form of MYC oncogenic stress, that we term RNA catabolic stress (RCS), can be exploited therapeutically by inhibiting HPRT1, which removes the compensatory nucleotide salvage pathway that enables cancer cells to tolerate RCS.

MYC has been known to induce ROS for two decades and oxidative stress has been suggested as a therapeutic vulnerability in MYC-driven cancers, though the mechanism by

which MYC induces oxidative stress is unclear (40). Our data indicate that MYC hyperactivation induces oxidative stress through increased RNA decay by the cytoplasmic exosome and downstream elevation in purine ribonucleotide catabolism by XDH. Given this novel understanding of MYC-induced oxidative stress, our results suggest the possibility of exacerbating oxidative stress-induced cell death in MYC-driven cancer by toggling RNA metabolism toward increased RNA degradation. Intriguingly, XDH inhibitor allopurinol is given as a supportive measure during chemotherapy which could inadvertently be helping MYC-driven tumor cells survive RCS. Further studies will be needed to understand whether other oncogenic contexts (e.g., oncogenic transcription factors like the estrogen receptor) produce aberrant ribonucleotide catabolism and oxidative stress through similar mechanisms.

Targeting DNA metabolism has been a mainstay in cancer therapeutics for more than 75 years, where rapidly replicating tumor cells exhibit enhanced sensitivity to chemotherapies that impede DNA synthesis, induce DNA damage, or inhibit DNA repair. Unfortunately, these therapies also impose undesired toxicity in actively dividing nonmalignant cells (like the immune compartment and GI tract), and these dose-limiting toxicities are often a major limitation to providing efficacious cancer treatment. For instance, the HPRT1 antagonist 6-MP is used to treat ALL and CML and is known to cause cytotoxicity through conversion into thio-GTP and activation of mismatch repair upon incorporation into DNA (72, 73). Our data suggest an alternative, proliferation-independent mechanism whereby 6-MP causes cancer cytotoxicity through increased ribonucleotide catabolism in MYC-driven malignancies. While this mechanism requires validation and further study, it invokes the provocative idea that therapies specifically targeting oncogenic stress due to enhanced RNA turnover may provide new entry points for cancer therapy. Development of new modalities that exploit this mechanism may provide new therapeutic approaches that avoid the toxicities associated with DNA poisons and perhaps even kill nondividing cancer cells.

METHODS

Vectors and Virus Production

Commercially available pGIPZ shRNAs targeting *DIS3L* (V2HS_99882 and V3LHS_391635), *EXOSC8* (V2LHS_ 61553 and V2HS_202870), *EXOSC2* (V3LHS_368199, V2HS_197390 and V2HS_6007), *XDH* (V2LHS_92691), and *HPRT1* (V2LHS_82409, V3LHS_364983 and V3LHS_364984) were obtained from Open Biosystems. shRNAs targeting the 3′ UTR region of *DIS3L* were designed using the RNAi-Central (http://katahdin.mssm.edu/siRNA/RNAi.cgi?type=shRNA) algorithm (shRNA sequence 5′- TGCTGTTGACAGTGAGCGAAGAG CGAGACTCCATCTCAAATAGTGAAGCCACAGATGTATTTG AGATGGAGTCTCGCTCTGTGCCTACTGCCTCGGA -3′). For inducible RNAi experiments, shRNAs were cloned into the pINDUCER11, and for inducible cDNA experiments, wild-type and mutant cDNAs were cloned into the pINDUCER22 doxycycline-inducible lentiviral expression system (75). BCL2-pcw107-V5 was a gift from David Sabatini and Kris Wood (Addgene plasmid # 64630; http://n2t.net/addgene:64630; RRID:Addgene_64630). DIS3L mutants were generated by site-directed mutagenesis using QuikChange II (Agilent) according to manufacturer's protocol. Lentiviruses and retroviruses were produced by transiently transfecting shRNA or cDNA constructs into HEK293T cells using Mirus Bio TransIT (Mirusbio) and viral supernatants were collected 48 hours after transfection.

Cell Culture

All cell lines were incubated at 37°C in 5% CO_2. MYC-ER HMECs were cultured in MEGM media (Lonza) and treated with 4 to 60 nM 4-OHT to induce MYC hyperactivation. MDA-MB-231 LM2 and 293T were cultured in DMEM media (Gibco) supplemented with 10% FBS. SUM159 were cultured in F12 media (Thermo Fisher) supplemented with 5% FBS, 10 mmol/L HEPES, 5 μg/mL insulin, and 1 μg/mL hydrocortisone. HCC1937 were cultured in RPMI 1640 media (Gibco) supplemented with 10% FBS. SKBR3 cells were cultured in McCoy's 5A medium (Corning) supplemented with 10% FBS. MYCN3 were cultured in RPMI 1640 media (Gibco) supplemented with 10% FBS and treated with 1 uμ/mL doxycycline to induce MYCN expression. For P493-6 cell line with pMYC-tet construct, MYC was reduced by treating cells with 0.1 mg/mL tetracycline (Sigma) for 72 hours. MYC was re-induced by washing P493-6 cells with PBC twice, then culturing cells in RPMI-1640 medium with 10% Tet System Approved FBS (Clontech) and 1% GlutaMAX. 293T, SKBR3, and HCC1937 cells were obtained from ATCC #cat nr. CRL-3216, HTB-30, and CRL-2336, respectively); SUM159 (female) cells were obtained from BioVT (SUM-159PT); MDA-MB-231-LM2 were obtained from (76); HMEC (HME1) cells were obtained from Infinity (hTERT-HME1); and MYC-ER HMEC (HME1 MYC-ER) were obtained from (10). Cells were tested for mycoplasma every 6 months. Last testing was done using MycoAlert kit (Lonza) in November 2022 and tested negative. Xanthosine (CDS020790), IMP (57510), and GMP (G8377) were purchased from Sigma (CDS020790).

Cell Line Generation

Stable cell lines (MYC-ER HMECs and breast cancer cell lines MDA-MB-231-LM2 and SUM159) expressing pGIPZ or cDNA constructs were generated by infecting cells at a multiplicity of infection of 0.3 (pGIPZ shRNA) or 0.5 (pINDUCER cDNA) in the presence of 8 μg/mL polybrene. Transduced cells with pGIPZ shRNA plasmid were selected using 1 μg/mL puromycin. Single cell clones were generated for cells transduced with pINDUCER22 plasmid containing cDNA.

Western Blotting and Antibodies

For Western blotting, cells were lysed in 1x Laemmli SDS sample buffer, incubated at 95°C for 10 minutes, centrifuged at 13,000 × *g*, and equal cell numbers were loaded onto criterian TGX stain-free precast gels (Bio-Rad) and separated by electrophoresis. Proteins were transferred on methanol-activated 0.45 μmol/L PVDF membrane (Thermo scientific) using semi-dry transfer by Trans-Blot (Bio-Rad). Following transfer, membrane was blocked in 5% BSA in TBS-T (0.1% Tween-20 in 1 × TBS) for 1 hour and incubated with primary antibody overnight at 4°C. The membrane was then washed three times in 1 × TBS-T and incubated with secondary antibody conjugated with fluorophore for 1 hour at room temperature. Following secondary antibody washing, membrane was imaged in respective fluorescence channel using chemi-doc (Bio-Rad). Antibody for BCL2 was purchased from Cell Signaling (cat#4223; RRID: AB_1903909) and vinculin from Sigma (cat#V9131; RRID: AB_477629)

Cell Viability and Cell Death Assays

For cell death assays in MYC-ER HMECs in response to inhibition of purine salvage (using shHPRT1, 6-MP, or DA-XV-55), MYC was induced with 4 to 12 nmol/L 4-OHT to allow for observation of a MYC-synthetic lethal effect. For cell death assays in MYC-ER HMECs using all other shRNAs or cDNAs, MYC was induced with 60 nmol/L 4-OHT. For cell death assays using propidium iodide (PI), cells were seeded at a density of 20,000 onto 12-well plates and 3,000 onto 96-well plates (Corning). MYC was induced the following day and 24 hours

after MYC hyperactivation, the supernatant from the cells was collected. Cells were then trypsinized, mixed with the previously collected supernatants, and stained with PI (2 μg/μL) for 5 minutes. PI-positive dead cells were analyzed by flow cytometry (BD LSRFortessa) or by imaging using the Celigo Imaging Cell Cytometer (Brooks).

For annexinV assay, cells were trypsinized and stained with annexinV-APC conjugates from Thermo Fisher (Cat#A35110) according to manufacturer's protocol. Stained cells were analyzed by flow cytometry (BD LSRFortessa).

For caspase-3/7 activity measurement, cells were cultured in white-walled 96-well plate (Corning) in 100 μL cell culture media. The next day, 100 μL Caspase-Glo 3/7 reagent (Promega, G8090) was added to the cell media, mixed briefly, and incubated in the dark for 30 to 60 minutes. Luminescence was measured on a luminometer (Molecular Devices). Luminescence readings were normalized to cell number determined by Hoechst 33342 (Life Technologies) staining of a duplicate 96-well plate (Greiner), followed by nuclei counting using the Celigo Imaging Cell Cytometer (Brooks).

For anchorage-independent growth assays, breast cancer cells were suspended in 0.3% low-melting agarose (Invitrogen) and plated on already solidified 0.5% low-melting agarose in culture medium. Media were changed every 3 days and macroscopic colonies (>125 μmol/L) were quantified after 2 weeks in respective treatment conditions.

For MTT assays, cancer cells MDA-MB-231-LM2 (LM2), SUM159, P493-6, MYCN3, SKBR3, and HCC1937 were seeded at a density of 3,000 onto 96-well plates (Greiner). After 6-MP treatment, cells were fixed and stained with MTT solution, lysed in 150 μL DMSO, and OD was measured at 550 nmol/L.

RNA Isolation and qRT–PCR

RNA isolation was performed with the RNeasy Mini kit (Qiagen) and TRIzol method (Invitrogen). Reverse transcription was performed using the High Capacity RNA-to-cDNA Master Mix (Applied Biosystems), and qPCR was performed using SYBR Green MasterMix (Applied Biosystems). qPCR primers were designed from PrimerBank (https://pga.mgh.harvard.edu/primerbank/; ref. 77). The following primers were used: *DIS3L* forward: 5′-GCCCACGAGCTTTGTGATTCT-3′, reverse: 5′-GCTGGCTCCTTGAAGTCGAA-3′; *EXOSC8* forward: 5′-ACCCCTGTGTTCATCGAGATT-3′, reverse: 5′-CATCGTAGTCGAGGCAAATGAG-3′; *EXOSC2* forward:

5′-CAATCACTACGGACACAGGATTC-3′, reverse: 5′-TTCGTCCCACTACGATGTCTC-3′; ACTB forward: 5′-TCCCTGGAGAAGAGCTACCAG-3′, reverse: 5′-TCGATGCCACAGGACTCCAT-3′; *XDH* forward: 59-CCAAATTGCTGCATGAACCAG-3′, reverse: 5′-TGCTTCCGAGGAGTGTCTTTC-3′; *HPRT1* forward: 5′- CCTGGCGTCGTGATTAGTGAT-3′, reverse 5′-AGACGTTCAGTCCTGTCCATAA-3′.*PVRL4* forward: 5′- GGAGGAGAGTGTAGGGCTGA-3′, reverse 5′- CGTGGTCAGCGTGGAGTAAC-3′.

Sample Preparation for Mass Spectrometry and Metabolomics Analysis

Metabolites were extracted from the cells and quality controls as following. For cell lines with the indicated genotypes, 1 to 3 × 10^6 cells were trypsinized, washed with 1x PBS, centrifuged, and snap frozen in liquid nitrogen. For metabolite extraction, frozen cell pellets were thawed at 4°C and were subjected to three freeze–thaw cycles on liquid nitrogen and ice, to rupture the cell membrane. Next, 750 μL ice-cold methanol:water (4:1) containing 20 μL spiked internal standards were added to each cell extract. Next, ice-cold chloroform and water were added in a 3:1 ratio to make a final proportion of 4:3:2 (methanol:chloroform:water). The organic (methanol and chloroform) and aqueous layers were dried and resuspended in 50:50 methanol:water. Next, the extracts were deproteinized using a 3-kDa molecular filter (Amicon Ultracel-3K Membrane; Millipore Corporation) and the filtrate containing the metabolites was dried under vacuum (Genevac EZ-2plus; Gardiner). Prior to mass spectrometry, the dried extracts were resuspended in identical volumes of injection solvent composed of 1:1 water:methanol and subjected to liquid chromatography-mass spectrometry (32, 78).

Liquid Chromatography-Mass Spectrometry

A total of 10 μL of suspended samples was injected and analyzed using a 6490 triple-quadrupole mass spectrometer (Agilent Technologies, Santa Clara, CA) coupled to an HPLC system (Agilent Technologies, Santa Clara, CA) via single reaction monitoring of the selected metabolites. Source parameters were as follows: gas temperature was 250°C; gas flow was 14 L/min; nebulizer was 20psi; sheath gas temperature was 350°C; sheath gas flow was 12 L/min; capillary was 3000 V positive and 3000 V negative; nozzle voltage was 1500 V positive and 1500 V negative. Approximately 8 to 11 data points were acquired per detected metabolite.

Method 1. ESI positive mode was used in method A. The HPLC column was Waters XBridge Amide 3.5 μm, 4.6 × 100 mm. Mobile phase A and B were 0.1% formic acid in water and acetonitrile respectively. Gradient: 0 minute, 85% B; 3–12 minutes, 85% to 10% B, 12–15 minutes, 10% B, 16 minutes, 85% B, followed by re-equilibration end of the gradient, the 23 minutes to the initial starting condition 85% B. Flow rate: 0.3 mL/minutes.

Method 2. For reverse phase separation, a Zorbax Eclipse XDB-C18 column (50 × 4.6 mm i.d.; 1.8 μm particle size, Agilent Technologies, Santa Clara, CA) maintained at 37°C, was used. The mobile phase used for the reverse phase separation contained 0.1% formic acid/water (v/v; A) and 0.1% formic acid/acetonitrile (v/v; B). The gradient conditions were 0 to 6 minutes, 2% B; 6.5 minutes, 30% B; 7 minutes, 90% B; 12 minutes, 95% B; followed by re-equilibration to the initial starting condition.

Normalization. Metabolite peak areas were normalized to the internal standard metabolite peak area and log-transformed (base 2) to obtain the relative metabolite abundance.

Microscopy

EU Labeling Assay. MYC-ER HMECs engineered with DIS3L or control shRNA ±60 nmol/L 4-OHT were labeled with 1 mmol/L EU for 1 hour and fixed in 4% paraformaldehyde (PFA). For chase experiment, fresh media without EU but containing 2 μg/mL ActinomycinD was added to the cells. Cells were harvested 2 to 3 hours post chase by fixing in 4% PFA. EU Click-iT staining was performed according to manufacturer's instructions (Thermo Fisher). EU signal was visualized by fluorescence microscopy and multiple images were collected using Nikon Eclipse Ti-E inverted microscope with 20X air objective and Andor Zyla 4.2 sCMOS camera. Fluorescence intensity for each cell was analyzed using NIS-Element AR 4.30 software. For each image, EU signal intensity was adjusted for background fluorescence by subtracting the mean extracellular pixel value.

ROS Measurement. HMEC cells engineered with DIS3L, XDH, or control shRNA ±60 nmol/L 4-OHT or ±6-MP were incubated with CellROX Deep Red reagent at a final concentration of 5 μmol/L (life technologies) for 30 minutes at 37°C. Cells were washed three times with PBS and fixed with 4% formaldehyde for 15 minutes. Fixed cells were visualized and imaged using a Nikon Ti-E inverted microscope with 20X air objective and Andor Zyla 4.2 sCMOS camera. For each treatment condition, cells were analyzed for mean DeepRed fluorescence intensity using NIS-Element AR 4.30 software. For each image, CellROX DeepRed signal intensity was adjusted for background fluorescence by subtracting the mean extracellular pixel value.

In Vitro *Competition Assay*

LM2 and SUM159 cells engineered with pINDUCER11-shDIS3L or control shRNA, which allows doxycycline-inducible shRNA and red fluorescence protein (RFP) expression. Each cell population was mixed with non-RFP LM2 or SUM159 cells. Mixed population was treated with increasing doses of 6-MP or DA-XV-55 and the proportion of shRNA expressing (RFP+) cells was analyzed by flow cytometry (BD LSRFortessa).

Pooled In Vivo *Tumor Competition Assay*

LM2 breast cancer cells were individually transduced with shRNAs (targeting RNA metabolism and nucleotide salvage genes) in pINDUCER11 backbone (75) at a multiplicity of infection of 1.2 to 1.5. All cell lines were sequentially pooled in equal ratios. The pool of cells was then subcutaneously transplanted (3×10^6 cells per mice) into athymic nude mice (female mice, 4–6 weeks old, Harlan labs). Mice were randomized onto water with or without doxycycline (±DOX) 3 days post-transplantation. Tumors were measured using calipers and harvested at 1,000 mm^3. Genomic DNA from dissected tumors was collected using the QIAamp DNA mini kit (Qiagen). Genomic DNA from tumor samples was isolated and shRNA library was amplified with the following primers: Forward: 5′- TCGTCGGCAGCGTC AGATGTGTATAAGAGACAG TAG TGA AGC CAC AGA TGT A-3′, reverse: 5′- GTCTCGTGGGCTCGGAGATGTGTATAAGAGACAGGG CGCGGAGGCCAGATCTT-3′. Amplified shRNA library obtained from each tumor was indexed using Nextera Index Kit (96 indices) from Illumina and purified using PippinHT. Library was quantified using KAPA Library Quantification Kit and sequenced on Illumina HiSeq 2500 platform (~10×10^6 reads per tumor with a read coverage of >10,000 reads per shRNA per tumor).

Reads were processed to remove adaptor sequences using cutadapt (79) and then aligned to the reference library using Bowtie2 (80) in end-to-end mode allowing up to a maximum of three mismatches/indels compared to the reference sequence. The raw number of reads mapping to each shRNA in each sample was then extracted from the SAM files and DESeq2-v.1.14.0 (81) was used to determine the normalized abundance of each shRNA in the vehicle and doxycycline-treated tumors.

Investigators responsible for monitoring and measuring the xenografts of individual tumors were not blinded. Simple randomization was used to allocate animals to experimental groups. All animal studies were performed in accordance with institutional and national animal regulations. Animal protocols were approved by the Institutional Animal Care and Use Committee at Baylor College of Medicine. Power analysis was used to determine appropriate sample size to detect significant changes in animal survival, which were based on previous survival analyses in our laboratory. All animals were included in analyses.

RNA Sequencing

Total RNA (1 ug/sample) was used as input for the NEBNext rRNA Depletion Kit (Human/Mouse/Rat; NEB). After rRNA depletion, libraries were made using the NEBNext Ultra Directional RNA Library Prep Kit for Illumina, quantified using KAPA Library Quantification Kit, and sequenced on the NextSeq 500/550. After demultiplexing, reads were processed using SAMtools (v1.4) and aligned using Hisat2 (v2.0.4) with default parameters. The reference genome sequences (hg38/GRCh38) and gene annotation files were obtained from the UCSC Genome Browser. Gene expression FPKM values used for differential gene expression analyses were obtained using the cufflinks suite (v2.2.1). Analysis of gene expression deciles and plots were made using R (v4.0.3). RNA sequencing data for this experiment are deposited to the Gene Expression Omnibus (GEO) repository with the GEO accession nr. GSE223046.

Mutation and Structure Analysis for DIS3L

The relative evolutionary importance of DIS3L residues was estimated by the ET method using homologous sequences with MUSCLE (65). The ET method computed importance rankings by systematically correlating residue variations with evolutionary divergences, in effect linking perturbations in sequence with perturbations in function as judged by phylogenetic distances. TCGA database was used to obtain mutation information on DIS3L residues. The impact of amino acid substitutions was estimated using the EA equation (65). ET ranks were aligned and colored onto the crystal structure of the human DIS3L homolog, *Saccharomyces cerevisiae* Dis3 (PDB ID 4IFD, chain J; ref. 66), using PyETV (PMID: 20929911). The Dis3 G833S mutation (G786S in DIS3L) was modeled using the serine rotamer with the least clashing in Coot (82). Figures were prepared with the PyMol visualization software (The PyMOL Molecular Graphics System, version 2.4.2 Schrödinger).

Statistical Analysis

All experiments were performed on biological replicates ($n \geq 3$) unless otherwise specified. Sample sizes for experimental groups and conditions are reported in the appropriate figure legends and methods. For cell culture experiments, sample size was not predetermined, and all samples were included in analyses.

Principal component analysis was performed on the catabolite data from Terunuma and colleagues (32) measuring the levels of 22 catabolites across 61 samples. A linear model was used to assess significance of the association between principal component 1 and MYC status.

For comparison of control and experimental groups, significance was determined using two-tailed unpaired Student *t* test unless otherwise specified in figure legends. Data were checked for similar variance before statistical analysis.

Purine Catabolism Model

Predictions of hypothetical purine nucleotide flux (Supplementary Table S4) were developed using the published model (46, 47). The model was implemented as described except for several corrections necessary to match the reported steady state; the corrections, code to match the results in the original study (46), and code to create the figures in this paper, are available upon request. After running to steady state, we modeled addition of 25% of either RNA, over the course of 1 day, while allowing the model to relax back to steady state; the addition was in the form of a beta function to represent additional production due to MYC hyperactivation, with peak addition occurring around 5 to 8 simulated hours after starting the run. Implementation was in R using the routine "ode" from the package "deSolve" (83), with the default options.

TCGA Data Analysis

Expression, copy number, and mutation data from TCGA were downloaded using TCGAbiolinks (84). RSEM normalized gene expression data from TCGA was obtained from the Broad GDAC Firehose. Copy number was obtained from TCGA as GISTIC data (85). Copy number analysis was done by segregating tumors based on a GISTIC score of >0 ("gain") or 0 ("normal") or <0 ("Loss").

Gene Ontology Analysis

For gene ontology enrichment analysis, MYC-synthetic viable candidates ($n = 223$ genes) from the genome-wide screen were analyzed using PANTHER (http://pantherdb.org/; ref. 86) for enrichment using the C2 cellular component database. Overrepresentation was determined using a binomial test with FDR correction.

Data Availability

Requests for resources and reagents should be directed to T.F. Westbrook (thomasw@bcm.edu) and J.K. Meena (meena@bcm.edu). RNA sequencing data are deposited to the GEO with the accession number GSE223046. Metabolomics data related to Fig. 1A are published and available to the reader (32). Other data and codes used in this study are available upon request.

Notes

Description of specific terms used in this manuscript: Ribonucleotide catabolism, Catalytic breakdown of nucleotides containing ribose sugar; RNA catabolites, nucleotide base containing metabolites resulting from RNA degradation; MYC hyperactivation, increasing the levels of MYC protein in nucleus to supraphysiological levels; Oncogenic MYC, levels/activity of MYC that are associated with human cancer; MYC-dependent cells, cell lines that require MYC for cell growth; MYC-independent cells, cell lines that do not require MYC for cell growth.

Authors' Disclosures

J.K. Meena reports grants from Susan G. Komen during the conduct of the study; personal fees from Affirmativ Diagnostics DBA ADx Health outside the submitted work. E.A. Bowling reports grants from NIH/NCI during the conduct of the study. K. Eagle reports personal fees from Flare Therapeutics and personal fees from Dana Farber Cancer Institute outside the submitted work. A.D. Yang reports grants from CPRIT and NIH/NCI during the conduct of the study. S.J. Kurley reports grants from CDMRP and The Helis Foundation during the conduct of the study; personal fees from Optum Genomics (UnitedHealth Group) and personal fees from Castle Biosciences outside the submitted work. C.M. Olson reports personal fees from Marlinspike Therapeutics outside the submitted work. K.L. Meerbrey reports personal fees from Marlinspike Therapeutics outside the submitted work. A. Sreekumar reports grants from Agilent Foundation, non-financial support from Sri Sathya Sai Institute for Higher Learning, India, and personal fees from Karkinos Health Care Pvt. Ltd., India, outside the submitted work. D. Rejman reports grants from The Ministry of Education, Youth and Sports during the conduct of the study. C.Y. Lin reports other support from Kronos Bio outside the submitted work. M.C. Pillon reports grants from Cancer Prevention & Research Institute of Texas, National Institute of Environmental Health Sciences, and National Institute of General Medical Sciences during the conduct of the study. T.F. Westbrook reports grants, personal fees, and other support from Marlinspike Therapeutics outside the submitted work. No disclosures were reported by the other authors.

Authors' Contributions

J.K. Meena: Conceptualization, data curation, software, formal analysis, supervision, validation, investigation, visualization, methodology, writing–original draft, project administration, writing–review and editing, This author is also a co-corresponding author on this manuscript. **J.H. Wang:** Data curation, software, formal analysis, validation, investigation, visualization, methodology, writing–original draft, writing–review and editing. **N.J. Neill:** Software, formal analysis, investigation, methodology, writing–review and editing. **D. Keough:** Resources, writing–review and editing. **N. Putluri:** Formal analysis. **P. Katsonis:** Software, formal analysis, writing–review and editing. **A.M. Koire:** Formal analysis. **H. Lee:** Investigation. **E.A. Bowling:** Investigation, writing–review and editing. **S. Tyagi:** Investigation. **M. Orellana:** Investigation. **R. Dominguez-Vidaña:** Software, formal analysis. **H. Li:** Software, formal analysis. **K. Eagle:** Software, formal analysis. **C. Danan:** Data curation, software, formal analysis. **H.-C. Chung:** Investigation, writing–review and editing. **A.D. Yang:** Investigation. **W. Wu:** Investigation. **S.J. Kurley:** Investigation. **B.M. Ho:** Formal analysis. **J.R. Zoeller:** Formal analysis, writing–review and editing. **C.M. Olson:** Investigation. **K.L. Meerbrey:** Investigation. **O. Lichtarge:** Formal analysis. **A. Sreekumar:** Investigation. **C.C. Dacso:** Resources, supervision, funding acquisition. **L.W. Guddat:** Resources, writing–review and editing. **D. Rejman:** Resources. **D. Hocková:** Resources. **Z. Janeba:** Resources, writing–review and editing. **L.M. Simon:** Data curation, software, formal analysis. **C.Y. Lin:** Data curation, software, formal analysis, writing–review and editing. **M.C. Pillon:** Software, formal analysis, writing–review and editing. **T.F. Westbrook:** Conceptualization, resources, data curation, formal analysis, supervision, funding acquisition, visualization, methodology, writing–original draft, project administration, writing–review and editing.

Acknowledgments

J.K. Meena is supported by Susan G. Komen PDF Basic/Translational and Clinical Funding Program (PDF17487931). A.D. Yang is supported by NIH/NCI Ruth L. Kirschstein National Research Service Award (NRSA) Individual Fellowship (1F30CA278316-01). J.R. Zoeller is supported in part by Baylor Research Advocates for Student Scientists. D. Rejman is supported by The Project National Institute Virology and Bacteriology (Programme EXCELES, Project No. LX22NPO5103) grants from the European Union-Next Generation EU. J.H. Wang is supported in part by Baylor Research Advocates for Student Scientists. E.A. Bowling is supported in part by Baylor Research Advocates for Student Scientists and the NIH (T32GM120011). M.C. Pillon is supported by the Cancer Prevention & Research Institute of Texas grant (CPRIT, RR200076), the National Institute of Environmental Health Sciences (NIEHS, R00ES030735), and the National Institute of General Medical Sciences (NIGMS, R35GM147123). This project was supported in part by the following Advanced Technology Cores at Baylor College of Medicine: the Cytometry and Cell Sorting Core with funding from CPRIT Core Facility Support Award (CPRIT-RP180672), NCI P30 Cancer Center Support Grant (CA125123), and NIH (RR024574), the Metabolomics Core at Baylor College of Medicine with funding from the CPRIT Core Facility Support Award (RP210227), NIH (P30 CA125123), and Dan L. Duncan Cancer Center, and the Integrated Microscopy Core with funding from NIH (DK56338 and CA125123), CPRIT (RP150578 and RP170719), the Dan L. Duncan Comprehensive Cancer Center, and the John S. Dunn Gulf Coast Consortium for Chemical Genomics. C.Y. Lin is supported by the Cancer Prevention Research Institute of Texas (RR150093), the NIH, and NCI (1R01CA215452-01), and is a Pew-Stewart Scholar for Cancer Research (Alexander and Margaret Stewart Trust). C.C. Dacso is supported by Philip J. Carroll Excellence Fund, Rene and Kay Joyce Family Foundation, Flour Family Foundation. J.H. Wang and T.F. Westbrook are supported in part by The McNair Medical Institute (The Robert and Janice McNair Foundation). T.F. Westbrook is supported by the NIH and NCI (U01CA214125, 1R01CA215226, and 1R01CA215452), DOD (1W81XWH-18-1-0573), The Welch Foundation (Q-0007), Merck KgaA Open Innovation Program, and the CRUK Grand Challenge and the Mark Foundation for Cancer Research (C5470/A27144 to T.F. Westbrook as a member of the SPECIFICANCER Team).

Note

Supplementary data for this article are available at Cancer Discovery Online (http://cancerdiscovery.aacrjournals.org/).

Received July 21, 2022; revised September 12, 2023; accepted May 6, 2024; published first September 3, 2024.

REFERENCES

1. Hanahan D, Weinberg RA. Hallmarks of cancer: the next generation. Cell 2011;144:646–74.
2. Hanahan D, Weinberg RA. The hallmarks of cancer. Cell 2000;100:57–70.

3. Lien EC, Lyssiotis CA, Cantley LC. Metabolic reprogramming by the PI3K-Akt-mTOR pathway in cancer. Recent Results Cancer Res 2016;207:39–72.
4. Düvel K, Yecies JL, Menon S, Raman P, Lipovsky AI, Souza AL, et al. Activation of a metabolic gene regulatory network downstream of mTOR complex 1. Mol Cell 2010;39:171–83.
5. Sullivan LB, Gui DY, Van Der Heiden MG. Altered metabolite levels in cancer: implications for tumour biology and cancer therapy. Nat Rev Cancer 2016;16:680–93.
6. Marcotte R, Sayad A, Brown KR, Sanchez-Garcia F, Reimand J, Haider M, et al. Functional genomic landscape of human breast cancer drivers, vulnerabilities, and resistance. Cell 2016;164:293–309.
7. Luo J, Solimini NL, Elledge SJ. Principles of cancer therapy: oncogene and non-oncogene addiction. Cell 2009;136:823–37.
8. Dang CV. MYC, metabolism, cell growth, and tumorigenesis. Cold Spring Harb Perspect Med 2013;3:a014217.
9. Herold S, Herkert B, Eilers M. Facilitating replication under stress: an oncogenic function of MYC? Nat Rev Cancer 2009;9:441–4.
10. Kessler JD, Kahle KT, Sun T, Meerbrey KL, Schlabach MR, Schmitt EM, et al. A SUMOylation-dependent transcriptional subprogram is required for Myc-driven tumorigenesis. Science 2012;335:348–53.
11. Liu L, Ulbrich J, Müller J, Wüstefeld T, Aeberhard L, Kress TR, et al. Deregulated MYC expression induces dependence upon AMPK-related kinase 5. Nature 2012;483:608–12.
12. David CJ, Chen M, Assanah M, Canoll P, Manley JL. HnRNP proteins controlled by c-Myc deregulate pyruvate kinase mRNA splicing in cancer. Nature 2010;463:364–8.
13. Guccione E, Martinato F, Finocchiaro G, Luzi L, Tizzoni L, Dall' Olio V, et al. Myc-binding-site recognition in the human genome is determined by chromatin context. Nat Cell Biol 2006;8:764–70.
14. Herkert B, Eilers M. Transcriptional repression: the dark side of myc. Genes Cancer 2010;1:580–6.
15. Wiese KE, Walz S, von Eyss B, Wolf E, Athineos D, Sansom O, et al. The role of MIZ-1 in MYC-dependent tumorigenesis. Cold Spring Harb Perspect Med 2013;3:a014290.
16. Muhar M, Ebert A, Neumann T, Umkehrer C, Jude J, Wieshofer C, et al. SLAM-seq defines direct gene-regulatory functions of the BRD4-MYC axis. Science 2018;360:800–5.
17. Walz S, Lorenzin F, Morton J, Wiese KE, von Eyss B, Herold S, et al. Activation and repression by oncogenic MYC shape tumour-specific gene expression profiles. Nature 2014;511:483–7.
18. Eilers M, Eisenman RN. Myc's broad reach. Genes Dev 2008;22:2755–66.
19. Sabò A, Amati B. Genome recognition by MYC. Cold Spring Harb Perspect Med 2014;4:a014191.
20. Iritani BM, Eisenman RN. c-Myc enhances protein synthesis and cell size during B lymphocyte development. Proc Natl Acad Sci U S A 1999;96:13180–5.
21. Grandori C, Gomez-Roman N, Felton-Edkins ZA, Ngouenet C, Galloway DA, Eisenman RN, et al. c-Myc binds to human ribosomal DNA and stimulates transcription of rRNA genes by RNA polymerase I. Nat Cell Biol 2005;7:311–8.
22. Barna M, Pusic A, Zollo O, Costa M, Kondrashov N, Rego E, et al. Suppression of Myc oncogenic activity by ribosomal protein haploinsufficiency. Nature 2008;456:971–5.
23. Cunningham JT, Moreno MV, Lodi A, Ronen SM, Ruggero D. Protein and nucleotide biosynthesis are coupled by a single rate-limiting enzyme, PRPS2, to drive cancer. Cell 2014;157:1088–103.
24. Mannava S, Grachtchouk V, Wheeler LJ, Im M, Zhuang D, Slavina EG, et al. Direct role of nucleotide metabolism in C-MYC-dependent proliferation of melanoma cells. Cell Cycle 2008;7:2392–400.
25. Nie Z, Hu G, Wei G, Cui K, Yamane A, Resch W, et al. c-Myc is a universal amplifier of expressed genes in lymphocytes and embryonic stem cells. Cell 2012;151:68–79.
26. Lin CY, Lovén J, Rahl PB, Paranal RM, Burge CB, Bradner JE, et al. Transcriptional amplification in tumor cells with elevated c-Myc. Cell 2012;151:56–67.
27. Patange S, Ball DA, Wan Y, Karpova TS, Girvan M, Levens D, et al. MYC amplifies gene expression through global changes in transcription factor dynamics. Cell Rep 2022;38:110292.
28. Ruggero D. The role of Myc-induced protein synthesis in cancer. Cancer Res 2009;69:8839–43.
29. Ruggero D, Pandolfi PP. Does the ribosome translate cancer? Nat Rev Cancer 2003;3:179–92.
30. Liu Y-C, Li F, Handler J, Huang CRL, Xiang Y, Neretti N, et al. Global regulation of nucleotide biosynthetic genes by c-Myc. PLoS One 2008;3:e2722.
31. Huang F, Ni M, Chalishazar MD, Huffman KE, Kim J, Cai L, et al. Inosine monophosphate dehydrogenase dependence in a subset of small cell lung cancers. Cell Metab 2018;28:369–82.e5.
32. Terunuma A, Putluri N, Mishra P, Mathé EA, Dorsey TH, Yi M, et al. MYC-driven accumulation of 2-hydroxyglutarate is associated with breast cancer prognosis. J Clin Invest 2014;124:398–412.
33. Budczies J, Brockmöller SF, Müller BM, Barupal DK, Richter-Ehrenstein C, Kleine-Tebbe A, et al. Comparative metabolomics of estrogen receptor positive and estrogen receptor negative breast cancer: alterations in glutamine and beta-alanine metabolism. J Proteomics 2013;94:279–88.
34. Liao C, Glodowski CR, Fan C, Liu J, Mott KR, Kaushik A, et al. Integrated metabolic profiling and transcriptional analysis reveals therapeutic modalities for targeting rapidly proliferating breast cancers. Cancer Res 2022;82:665–80.
35. Eberhardy SR, Farnham PJ. Myc recruits P-TEFb to mediate the final step in the transcriptional activation of the cad promoter. J Biol Chem 2002;277:40156–62.
36. Brès V, Yoshida T, Pickle L, Jones KA. SKIP interacts with c-Myc and menin to promote HIV-1 Tat transactivation. Mol Cell 2009;36:75–87.
37. Bouchard C, Marquardt J, Brás A, Medema RH, Eilers M. Myc-induced proliferation and transformation require Akt-mediated phosphorylation of FoxO proteins. EMBO J 2004;23:2830–40.
38. Kanazawa S, Soucek L, Evan G, Okamoto T, Peterlin BM. c-Myc recruits P-TEFb for transcription, cellular proliferation and apoptosis. Oncogene 2003;22:5707–11.
39. Rahl PB, Lin CY, Seila AC, Flynn RA, McCuine S, Burge CB, et al. c-Myc regulates transcriptional pause release. Cell 2010;141:432–45.
40. Muthalagu N, Murphy DJ. Is oxidative stress MYC's Achilles heel? Cell Death Differ 2018;25:1189–90.
41. Chandriani S, Frengen E, Cowling VH, Pendergrass SA, Perou CM, Whitfield ML, et al. A core MYC gene expression signature is prominent in basal-like breast cancer but only partially overlaps the core serum response. PLoS One 2009;4:e6693.
42. Liberzon A, Birger C, Thorvaldsdóttir H, Ghandi M, Mesirov JP, Tamayo P. The molecular signatures database (MSigDB) hallmark gene set collection. Cell Syst 2015;1:417–25.
43. Lynch M, Marinov GK. The bioenergetic costs of a gene, Proc Natl Acad Sci U S A 2015;112:15690–5.
44. Traut TW. Physiological concentrations of purines and pyrimidines. Mol Cell Biochem 1994;140:1–22.
45. Lane AN, Fan TWM. Regulation of mammalian nucleotide metabolism and biosynthesis. Nucleic Acids Res 2015;43:2466–85.
46. Curto R, Voit EO, Sorribas A, Cascante M. Mathematical models of purine metabolism in man. Math Biosci 1998;151:1–49.
47. Pillwein K, Chiba P, Knoflach A, Czermak B, Schuchter K, Gersdorf E, et al. Purine metabolism of human glioblastoma in vivo. Cancer Res 1990;50:1576–9.
48. Martinon F, Pétrilli V, Mayor A, Tardivel A, Tschopp J. Gout-associated uric acid crystals activate the NALP3 inflammasome. Nature 2006;440:237–41.
49. Braga TT, Forni MF, Correa-Costa M, Ramos RN, Barbuto JA, Branco P, et al. Soluble uric acid activates the NLRP3 inflammasome. Sci Rep 2017;7:39884.
50. Zrenner R, Stitt M, Sonnewald U, Boldt R. Pyrimidine and purine biosynthesis and degradation in plants. Annu Rev Plant Biol 2006;57:805–36.
51. Hsu TY-T, Simon LM, Neill NJ, Marcotte R, Sayad A, Bland CS, et al. The spliceosome is a therapeutic vulnerability in MYC-driven cancer. Nature 2015;525:384–8.

52. Mi H, Ebert D, Muruganujan A, Mills C, Albou LP, Mushayamaha T, et al. PANTHER version 16: a revised family classification, tree-based classification tool, enhancer regions and extensive API Nucleic Acids Res 2021;49:D394–403.
53. Staals RHJ, Bronkhorst AW, Schilders G, Slomovic S, Schuster G, Heck AJR, et al. Dis3-like 1: a novel exoribonuclease associated with the human exosome. EMBO J 2010;29:2358–67.
54. Tomecki R, Kristiansen MS, Lykke-Andersen S, Chlebowski A, Larsen KM, Szczesny RJ, et al. The human core exosome interacts with differentially localized processive RNases: hDIS3 and hDIS3L. EMBO J 2010;29:2342–57.
55. Puno MR, Weick EM, Das M, Lima CD. SnapShot: the RNA exosome. Cell 2019;179:282e1.
56. Moore MJ. Nuclear RNA turnover. Cell 2002;108:431–4.
57. Thomas MP, Liu X, Whangbo J, McCrossan G, Sanborn KB, Basar E, et al. Apoptosis triggers specific, rapid, and global mRNA decay with 3′uridylated intermediates degraded by DIS3L2. Cell Rep 2015;11:1079–89.
58. Fanidi A, Harrington EA, Evan GI. Cooperative interaction between c-myc and bcl-2 proto-oncogenes. Nature 1992 359:554–6.
59. Bissonnette RP, Echeverri F, Mahboubi A, Green DR. Apoptotic cell death induced by c-myc is inhibited by bcl-2. Nature 1992;359:552–4.
60. Yang E, van Nimwegen E, Zavolan M, Rajewsky N, Schroeder M, Magnasco M, et al. Decay rates of human mRNAs: correlation with functional characteristics and sequence attributes. Genome Res 2003;13:1863–72.
61. Weber MJ. Ribosomal RNA turnover in contact inhibited cells. Nat New Biol 1972;235:58–61.
62. Yi X, Tesmer VM, Savre-Train I, Shay JW, Wright WE. Both transcriptional and posttranscriptional mechanisms regulate human telomerase template RNA levels. Mol Cell Biol 1999;19:3989–97.
63. Schwanhäusser B, Busse D, Li N, Dittmar G, Schuchhardt J, Wolf J, et al. Global quantification of mammalian gene expression control. Nature 2011;473:337–42.
64. Cerami E, Gao J, Dogrusoz U, Gross BE, Sumer SO, Aksoy BA, et al. The cBio cancer genomics portal: an open platform for exploring multidimensional cancer genomics data. Cancer Discov 2012;2:401–4.
65. Katsonis P, Lichtarge O. A formal perturbation equation between genotype and phenotype determines the Evolutionary Action of protein-coding variations on fitness. Genome Res 2014;24:2050–8.
66. Makino DL, Baumgärtner M, Conti E. Crystal structure of an RNA-bound 11-subunit eukaryotic exosome complex. Nature 2017;495:70–5.
67. Yang W. Nucleases: diversity of structure, function and mechanism. Q Rev Biophys 2011;44:1–93.
68. Vafa O, Wade M, Kern S, Beeche M, Pandita TK, Hampton GM, et al. c-Myc can induce DNA damage, increase reactive oxygen species, and mitigate p53 function: a mechanism for oncogene-induced genetic instability. Mol Cell 2002;9:1031–44.
69. KC S, Cárcamo JM, Golde DW. Antioxidants prevent oxidative DNA damage and cellular transformation elicited by the over-expression of c-MYC. Mutat Res 2006;593:64–79.
70. Morrish F, Neretti N, Sedivy JM, Hockenbery DM. The oncogene c-Myc coordinates regulation of metabolic networks to enable rapid cell cycle entry. Cell Cycle 2008;7:1054–66.
71. Harris CM, Massey V. The reaction of reduced xanthine dehydrogenase with molecular oxygen: reaction kinetics and measurement of superoxide radical. J Biol Chem 1997;272:8370–9.
72. Karran P, Attard N. Thiopurines in current medical practice: molecular mechanisms and contributions to therapy-related cancer. Nat Rev Cancer 2008;8:24–36.
73. Mathews CK. DNA synthesis as a therapeutic target: the first 65 years. FASEB J 2012;26:2231. 7.
74. Eng WS, Hocková D, Špaček P, Janeba Z, West NP, Woods K, et al. First crystal structures of *Mycobacterium tuberculosis* 6-oxopurine phosphoribosyltransferase: complexes with GMP and pyrophosphate and with acyclic nucleoside phosphonates whose prodrugs have antituberculosis activity. J Med Chem 2015;58:4822–38.
75. Meerbrey KL, Hu G, Kessler JD, Roarty K, Li MZ, Fang JE, et al. The pINDUCER lentiviral toolkit for inducible RNA interference *in vitro* and *in vivo*. Proc Natl Acad Sci U S A 2011;108:3665–70.
76. Minn AJ, Gupta GP, Siegel PM, Bos PD, Shu W, Giri DD, et al. Genes that mediate breast cancer metastasis to lung. Nature 2005;436:518–524.
77. Spandidos A, Wang X, Wang H, Seed B. PrimerBank: a resource of human and mouse PCR primer pairs for gene expression detection and quantification. Nucleic Acids Res 2010;38:D792–9.
78. Putluri N, Shojaie A, Vasu VT, Nalluri S, Vareed SK, Putluri V, et al. Metabolomic profiling reveals a role for androgen in activating amino acid metabolism and methylation in prostate cancer cells. PLoS One;2011;6:e21417.
79. Martin M. Cutadapt removes adapter sequences from high-throughput sequencing reads. EMBnet J 2011;17:10–2.
80. Langmead B, Salzberg SL. Fast gapped-read alignment with Bowtie 2. Nat Methods 2012 9:357–9.
81. Love MI, Huber W, Anders S. Moderated estimation of fold change and dispersion for RNA-seq data with DESeq2. Genome Biol 2014;15:550.
82. Emsley P, Lohkamp B, Scott WG, Cowtan K. Features and development of Coot. Acta Crystallogr D Biol Crystallogr 2010;66:486–501.
83. Soetaert K, Petzoldt T, Setzer RW. Solving differential equations in R: package deSolve. J Stat Softw 2010;33:1–25.
84. Colaprico A, Silva TC, Olsen C, Garofano L, Cava C, Garolini D, et al. TCGAbiolinks: an R/Bioconductor package for integrative analysis of TCGA data. Nucleic Acids Res 2016;44:e71.
85. Beroukhim R, Getz G, Nghiemphu L, Barretina J, Hsueh T, Linhart D, et al. Assessing the significance of chromosomal aberrations in cancer: methodology and application to glioma. Proc Natl Acad Sci U S A 2007;104:20007–12.
86. Thomas PD, Ebert D, Muruganujan A, Mushayahama T, Albou LP, Mi H. PANTHER: making genome-scale phylogenetics accessible to all. Protein Sci 2022;31:8–22.